Journal of South American Earth Sciences 168 (2025) 105828

Contents lists available at ScienceDirect

Journal of South American Earth Sciences

journal homepage: www.elsevier.com/locate/jsames

Carbon isotopic composition of CO_2 in interstitial soil gases from Southern Puna calderas, Central Andes: Decoding hydrothermal and shallow sources

A. Massenzio [a,b,*], M.C. Lamberti [a,b], A. Chiodi [c,d], I. Burgos [c,d], G. Viti [e,f], F. Tassi [e,f], M. Agusto [a,b], J. Viramonte [c,d]

[a] Universidad de Buenos Aires, Facultad de Ciencias Exactas y Naturales, Departamento de Ciencias Geológicas, Buenos Aires, Argentina
[b] CONICET – Universidad de Buenos Aires, Instituto de Estudios Andinos "Don Pablo Groeber" (IDEAN), Grupo de Estudio y Seguimiento de Volcanes Activos (GESVA), Buenos Aires, Argentina
[c] Instituto de Bio y Geociencias del NOA (IBIGEO, UNSa-CONICET), Salta, Argentina
[d] Universidad Nacional de Salta, Facultad de Ciencias Naturales, Salta, Argentina
[e] Institute of Geosciences and Earth Resources (IGG), National Research Council of Italy (CNR), Via G. La Pira 4, 50121, Florence, Italy
[f] Department of Earth Sciences, University of Florence, Via G. La Pira 4, 50121, Florence, Italy

ARTICLE INFO

Keywords:
Stable carbon isotopes
Soil CO_2 degassing
Volcanic hydrothermal systems
Cerro Blanco caldera
Cerro Galán caldera
Southern Puna calderas
Central Andes

ABSTRACT

The Southern Puna hosts active geothermal systems associated with various volcano-magmatic settings, among which caldera-hosted systems stand out as promising targets for geothermal exploration. This study focuses on two key calderas that currently exhibit active geothermal manifestations: Cerro Blanco Caldera (CBC), the youngest caldera system in the region (4.2 ka), and Cerro Galán Caldera (CGC), the largest caldera system in this sector of the Andes. The main objective was to decode the contributions of deep (hydrothermal) and shallow (biogenic and atmospheric) sources to diffuse CO_2 emitted from the soil, using a three-component mixing model. The results revealed the presence of these three sources: deep hydrothermal, shallow biogenic, and atmospheric. At CBC and CGC, high CO_2 concentrations (>5000 ppm) and $\delta^{13}C$-CO_2 values around −5 ‰ (vs. V-PDB) indicate a dominant hydrothermal contribution. In contrast, more ^{13}C-depleted values (down to −21.3 ‰) and lower CO_2 concentrations suggest microbial or soil respiration origin. Analysis of profiles in the soil revealed considerable variability, with deviations from the expected theoretical patterns in some cases. These anomalies are attributed to a combination of factors, including atmospheric contamination during sampling in low-permeability soils, isotopic fractionation under low gas flow conditions and local secondary processes, such as carbonate dissolution/precipitation. Despite these complexities, the combination of isotopic and concentration analysis robustly confirms the presence of hydrothermal CO_2 in the shallow soil gases in both calderas providing valuable insights for geothermal exploration and volcanic monitoring in the Central Andes.

1. Introduction

Gases diffusively released from the soil in volcanic and geothermal systems, which mainly consist of carbon dioxide (CO_2), are mostly invisible to the naked eye (Baubron et al., 1991; Chiodini et al., 1998). Potential soil CO_2 sources include: (i) deep volcanic-hydrothermal reservoirs, (ii) biogenic activity, and (iii) air (Chiodini et al., 1998, 2008; Capasso et al., 2001; Di Martino et al., 2016). The carbon isotopic composition of this gas (hereafter $\delta^{13}C$–CO_2) is widely used to distinguish and characterize deep volcanic-hydrothermal contributions from other origins, making this geochemical parameter useful in geothermal exploration and volcanic monitoring (e.g., Capasso et al., 1997; Chiodini et al., 2008; Viveiros et al., 2010; Lamberti et al., 2021a; 2025). In many cases, $\delta^{13}C$–CO_2 signatures reflect mixing among these three sources; however, they can also record secondary processes that overprint the primary isotopic signal (Simmons and Christenson, 1994, and references therein). These processes include isotopic fractionation associated with gas diffusion, carbonate precipitation/dissolution, partial CO_2 dissolution in shallow waters or soil pore waters, microbial activity and methanotrophy (Cerling et al., 1991; Capasso et al., 2001; Gilfillan et al., 2009; Barry et al., 2019; Vignoni et al., 2024; Wang et al., 2017). This overlap between mixing and overprinting processes makes the

This article is part of a special issue entitled: A Tribute to José Germán Viramonte published in Journal of South American Earth Sciences.

* Corresponding author. Universidad de Buenos Aires, Facultad de Ciencias Exactas y Naturales, Departamento de Ciencias Geológicas. Buenos Aires, Argentina.
E-mail address: massenzio.antonella@gmail.com (A. Massenzio).

https://doi.org/10.1016/j.jsames.2025.105828
Received 3 July 2025; Received in revised form 6 October 2025; Accepted 8 October 2025
Available online 15 October 2025

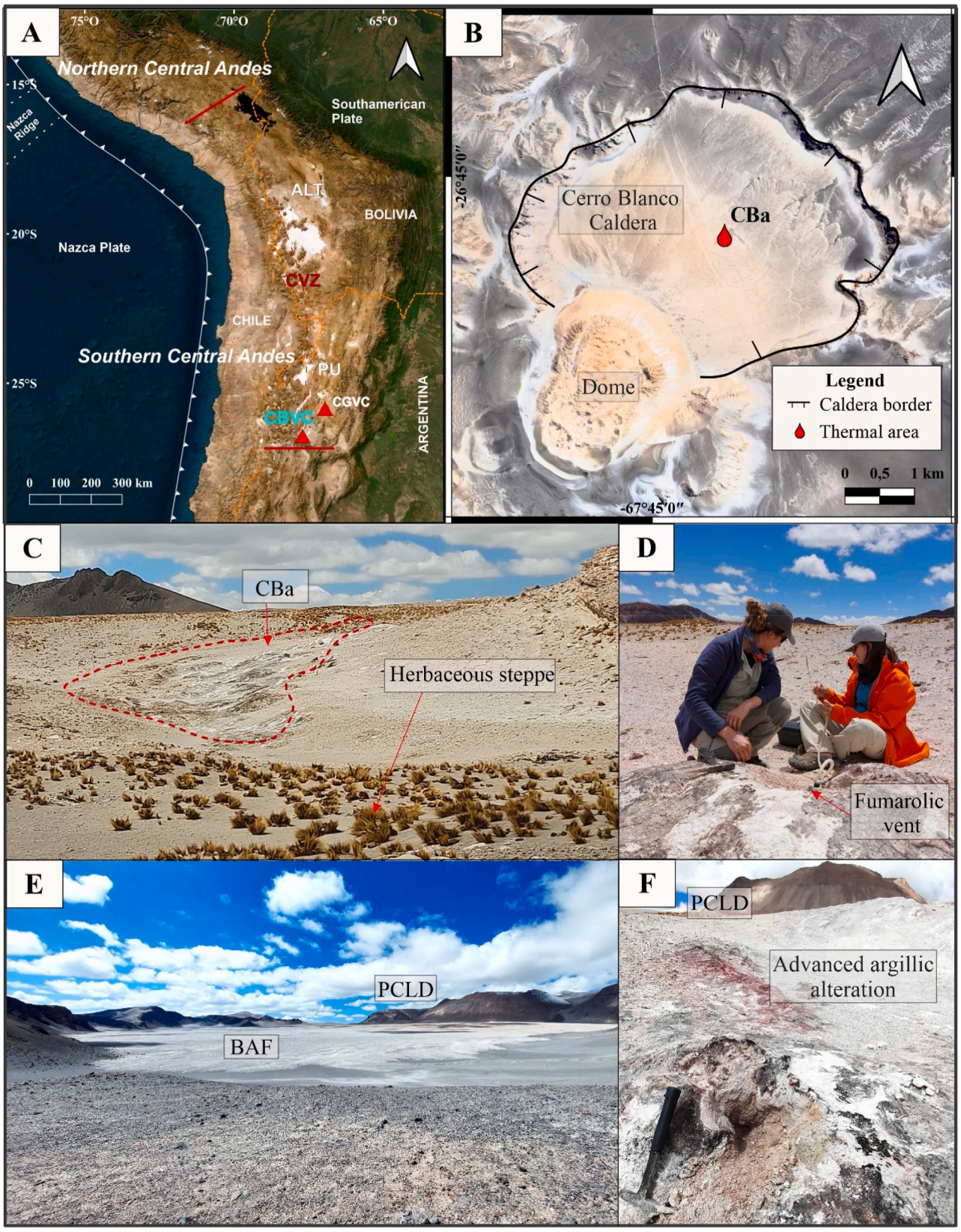

Fig. 1. A) Regional geotectonic setting of the caldera Cerro Blanco. CVZ: central volcanic zone. ALT: Altiplano. PU: Puna. CGCV: Cerro Galán Volcanic Complex. CBCV: Cerro Blanco Volcanic Complex. B) High resolution 3D image by Google Earth showing the main structural features and the location of the thermal area at CBC. C) General view of CBa, site where the geothermal fumaroles and the alteration zone occur. Characteristic vegetation within the caldera is also observed. D) Fumarolic vent at CBa. E) Panoramic view (toward SE) of the CBC, filled with block and ash flow deposits (BAF) and post-caldera lava domes (PCLD). F) Detailed view of hydrothermal alteration.

interpretation of isotopic values particularly challenging.

Several studies conducted in volcanic and geothermal environments worldwide have successfully applied the combined analysis of soil CO_2 flux, concentration, and $\delta^{13}C–CO_2$. This approach provides an estimation of the amount of deep-originated CO_2 and an integrated picture of the processes governing soil gas release. Such studies have been applied in different contexts, including Italy (Vulcano; Capasso et al., 1997; Mt. Etna, Vulcano, C. Calava, Camarda et al., 2007; La Solfatara volcano, Federico et al., 2010; Vulcano, Di Martino et al., 2016, 2020; Solfatara, Monterotondo Marittimo and Vulcano, Venturi et al., 2019), El Hierro in the Canary Islands (Melián et al., 2014), and other volcanic areas such as Long Valley Caldera (Lucic et al., 2015), among others. These works highlight both the potential and the challenges of using isotopic tracers in diffuse degassing studies, providing a broader framework for their application to Andean geothermal systems.

The Nazca-South American convergent margin presents promising opportunities for investigating the potential of unexplored geothermal resources, being characterized by geotectonic conditions favouring the occurrence of anomalous heat flux (>110 mW/m^2; Lucazeau, 2019). Despite the high geothermal potential, only one geothermal plant is currently operating in this region (Cerro Pabellón, Chile; Aravena et al., 2016). According to recent studies (Barcelona et al., 2017; Chiodi et al., 2019, 2024; Filipovich et al., 2022), the most promising high-temperature geothermal systems in Argentina occur in large size silicic calderas (Stimac et al., 2015) pertaining to the Neogene-Quaternary volcanic arc and back-arc of the Central and Southern Andes Volcanic Zones, such as Cerro Blanco and Cerro Galán calderas (CBC and CGC, respectively). Located in the southern Puna (northwest Argentina), these two calderas show hot springs, fumaroles, and areas marked by anomalously high diffuse CO_2 degassing suggesting the occurrence of well-developed hydrothermal systems, namely CBGS (Cerro Blanco geothermal system) and CGGS (Cerro Galán geothermal system) (Chiodi et al., 2019, 2024). Additionally, preliminary assessments of their geothermal potential emphasise the regional importance of these systems. For Cerro Blanco, calculations based on the volumetric method yielded values of ~1.1 × 10^{19} J (Chiodi et al., 2019), while an alternative approach considering the thermal energy associated with diffuse degassing resulted in ~2.37 kJ/s (Lamberti et al., 2021b). For Cerro Galán, volumetric estimations ranged between 2.09 MWe and 10.85 MWe, depending on the confidence level considered (Chiodi et al., 2024).

Previous studies on diffuse CO_2 fluxes from the soil at CBGS and CGGS (Lamberti et al., 2021b; Massenzio et al., 2024), based on Graphical Statistical Approach (GSA, Sinclair, 1974; Chiodini et al., 1998), suggested that the origin of CO_2 diffusively discharged from the soil was related to both magmatic degassing and shallow sources (e.g., microbial activity). To support them, the present study focuses on the composition of the stable carbon isotopes of CO_2 in interstitial gases from the soil as a key method to distinguish between deep and shallow fluid sources. We use the CO_2 concentrations and $\delta^{13}C–CO_2$ values to quantify the contributions of these sources through a three-component mixing model. By integrating isotopic data with CO_2 concentrations, collected at different depths, together with the fluxes, and soil temperature along soil profiles from CBC and CGC, we aim to elucidate both the origin of the CO_2 and the physicochemical processes controlling its degassing in these volcanic systems.

2. Geological setting and hydrothermal activity

2.1. Cerro Blanco caldera (CBC)

Cerro Blanco Caldera (26°S – 67°W) is the best-preserved volcanic structure of the Cerro Blanco Volcanic Complex (Fig. 1A), located in the back-arc region of the Central Volcanic Zone (~4200 m a.s.l.) (Seggiaro et al., 2000; Arnosio et al., 2005; Báez et al., 2020a, 2020b). It is ~4 km in diameter and composed mainly of rhyolitic to rhyodacitic rocks erupted from the Middle Pleistocene to Holocene. Its eruptive history includes large ignimbrite-forming eruptions (VEI ≥6), among the most significant of the Central Andes in the Holocene (Báez et al., 2015; Fernandez-Turiel et al., 2019).

CBC hosts an active and blind geothermal system (Chiodi et al., 2019; Lamberti et al., 2021b). Fumarolic discharges with outlet temperatures up to 93.7 °C, anomalous CO_2 diffuse degassing, and hydrothermal alteration deposits provide evidence of ongoing fluid circulation at depth. Fumarolic gases are dominated by H_2O and CO_2, with relevant amounts of H_2S, CH_4, and H_2. This activity takes place in a <1 km^2 hydrothermalized zone within the central sector of the CBC (Fig. 1B, C, D), named Cerro Blanco hydrothermal site (CBa). At this site, deposits of dilute pyroclastic density currents, breccias produced by phreatic explosions, and a 40 cm thick fossil silicic deposit suggest the occurrence of a more intense hydrothermal activity in the past (Fig. 1E and F; Viramonte et al., 2005a, 2005b). The silicic deposit consists of boehmite, kaolinite and alunite (Viramonte et al., 2005a). The hydrothermal reservoir, hosted in basement rocks, is a Na-Cl (HCO_3) aquifer with estimated silica-based temperatures of ~135 °C, recharged mainly by meteoric fluids but also receiving inputs from a degassing magma chamber, evidenced by a significant contribution of mantle He (39 %) and a $\delta^{13}C–CO_2$ value −5.23 ‰ in the fumarolic gas composition. The unconsolidated, fine-grained Cerro Blanco ignimbrite acts as a cap rock, with its low permeability enhanced by hydrothermal alteration, which likely seals the system (Chiodi et al., 2019).

2.1.1. Soil CO_2 diffuse degassing at CBC

Soil diffuse CO_2 is emitted through a single Diffuse Degassing Structure (DDS), mirroring a soil temperature anomaly up to 73 °C. Fluxes measured at CBC raised up to 320 g m^{-2} d^{-1} and their distribution on a logarithmic probability could be modelled by combining two log-normal populations, which according to the GSA suggests two different CO_2 sources (Lamberti et al., 2021b).

The high-flux population, constituting 12 % of the measured fluxes, had a mean value of approximately 135 ± 16 g m^{-2} d^{-1}. The low-flux population had a mean value of 10 ± 0.7 g m^{-2} d^{-1}, including the remaining 88 % of the measurements.

It should be noted that the terms “low flux population” and “high flux population” used in this study refer to local definitions, since soil CO_2 flux values in the Southern Puna calderas do not correspond to the conventional thresholds commonly adopted in other volcanic-hydrothermal contexts (e.g., average biogenic background values of ~30–40 g m^{-2} d^{-1} and volcanic-hydrothermal values up to 10^3–10^4 g m^{-2} d^{-1}). For this reason, and to avoid misleading associations, we follow the terminology previously adopted in our works and refer to low and high flux populations rather than to background and anomalous degassing.

An initial interpretation of this multiple sourcing of CO_2 suggests that the high-flux population is likely fed by an endogenous source (Lamberti et al., 2021b), based on the magnitude of these fluxes and their spatial correlation with the diffuse degassing structures (DDS) and thermal anomalies (Chiodini et al., 2001, 2005), as well as the geochemistry and isotopic composition of the fumaroles at Cerro Blanco (CBC) (Chiodi et al., 2019). The low-flux population, on the other hand, was recognized as “background” CO_2, mostly deriving from soil respiration.

Together, both log-normal flux populations contribute to a total diffuse CO_2 emission of 187 ± 17 kg d^{-1} across the mapped area (37,845.51 m^2). However, if the high-flux population is of endogenous origin, the geogenic CO_2 output in this area would be approximately 22 kg d^{-1} (Lamberti et al., 2021a). These low magnitude CO_2 emission was interpreted as resulting from an efficient sealing layer that limits gas escape.

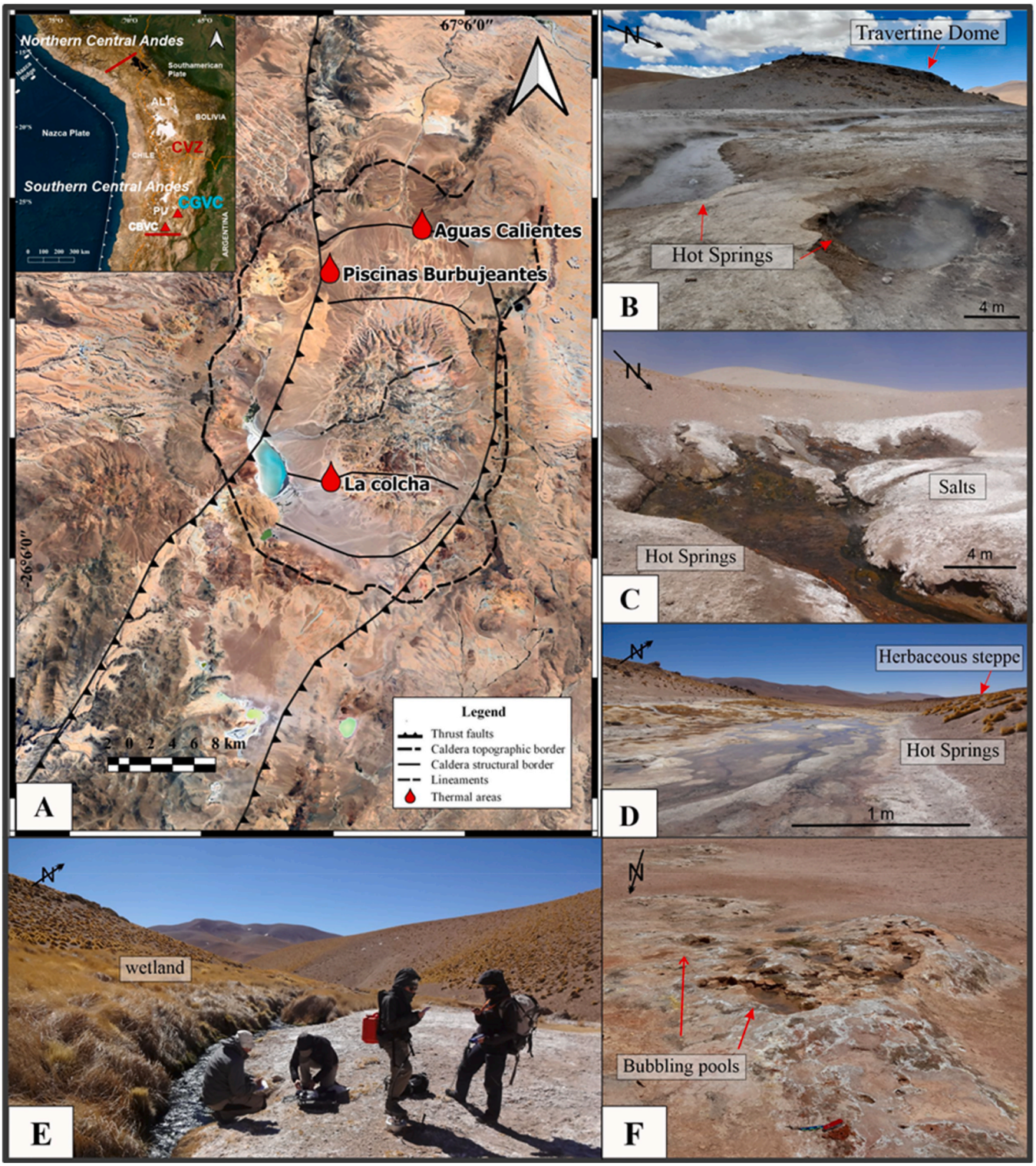

Fig. 2. A) High resolution 3D image by Google Earth showing the main structural features and the location of the thermal areas at GCC. Top left: regional geotectonic setting of the caldera. CVZ: central volcanic zone. ALT: Altiplano. PU: Puna. CGCV: Cerro Galán Volcanic Complex. CBCV: Cerro Blanco Volcanic Complex. B) Site within La Colcha's thermal area where hot springs gush with temperatures around 85 °C. A travertine dome and salt deposits can be observed. C) Another thermal site within La Colcha, featuring springs at the same temperature, is situated ~300 m from the previous site. Salt deposits are observed. D) Aguas Calientes thermal area. Sector where thermal springs gush out at 26 °C. E) Another thermal site within Aguas Calientes where springs with temperatures around 65 °C. F) Piscinas Burbujeantes thermal area. Bubbling pools and hydrothermal precipitates can be observed.

Table 1
Isotopic composition of soil CO_2 sampled at CBC and CGC.

Thermal Site	Profile Name	Sample Name	Depth (cm)	ΦCO_2 (g m^{-2} d^{-1})	Tsoil (°C)	[CO_2] (ppm)	$\delta^{13}C$-CO_2 (‰)
CBC							
CBa	CB1	CB1_V1	10	39.6	45.7	540	−15.4
		CB1_V2	20			750	−15.2
		CB1_V3	30			850	−11.7
	CB2	CB2_V1	10	27.9	36.6	>5000	−5.6
		CB2_V2	20			>5000	−4.9
	CB3	CB3_V1	10	22.5	48.2	>5000	−5.2
		CB3_V2	20			1300	−11.6
		CB3_V3	30			780	−14.3
CGC							
La Colcha	LC1	LC1_V1	10	2.5	25.5	400	−18.8
		LC1_V2	20			550	−19.6
	LC2	LC2_V1	10	1.0	29.5	600	−17.6
		LC2_V2	20			550	−17.8
		LC2_V3	30			700	−11.7
	LC3	LC3_V1	10	9.1	23	400	−19.7
		LC3_V3	30			600	−20.3
		LC3_V4	40			650	−13.2
	LC4	LC4_V1	10	35.3	22.5	>5000	−5.2
	LC5	LC5_V1	10	0.78	22.7	1000	−5.8
		LC5_V3	30			700	−9.8
		LC5_V4	40			600	−14.3
	LC6	LC6_V1	10	0.95	24.1	600	−15.7
		LC6_V2	20			650	−14.8
		LC6_V3	30			600	−15.1
Piscinas Burbujeantes	PBG1	PBG1_V1	10	3.0	61	370	−21.3
		PBG1_V2	20			700	−18.8
		PBG1_V3	30			670	−15.4
	PBG2	PBG2_V1	10	0.97	31.1	710	−13.3
		PBG2_V2	20			680	−14.6
		PBG2_V3	30			630	−18.8
Aguas Calientes	AC1	AC1_V1	10	4.39	26	>5000	−6.5
		AC1_V2	20			370	−17.9
		AC1_V3	30			700	−13.1
	AC2	AC2_V1	10	3.63	21.3	600	−17.6
		AC2_V2	20			700	−15.6
		AC2_V3	30			700	−15.9

2.2. Cerro Galán caldera (CGC)

Cerro Galán Caldera (Fig. 2; 25°49′–26°7′S, 67°5′W) is one of the largest resurgent calderas of the Central Andes, formed during a major supereruption at ~2 Ma that emplaced the Cerro Galán Ignimbrite (~630 km^3; Folkes et al., 2011a). With dimensions of 27 × 16 km and elevations up to 6000 m a.s.l., the CGC is structurally controlled by regional and local faults that also influence present-day fluid circulation. Several geophysical studies have imaged a partially molten body in the mid-crust named as the "Cerro Galán magma body", indicating ongoing magmatic input beneath the system (Bianchi et al., 2013; Calixto et al., 2013; Heit et al., 2014; Liang et al., 2014; Delph et al., 2017; Ward et al., 2017).

Three areas of surface thermal activity, known as La Colcha, Aguas Calientes, and Piscinas Burbujeantes del Galán, occur within the CGC. These areas host hot springs, bubbling pools and fumaroles (UNSa, 1982; Chiodi et al., 2024). At La Colcha and Aguas Calientes, the thermal waters have a Na^+-Cl^- composition with temperatures ranging between 25 and 85 °C and a slightly acidic to neutral pH (Fig. 2C, D, E y F). Diffuse CO_2 degassing from the soils occurs close to the thermal waters. Additionally, significant salt deposits, mainly consisting of calcite and halite, were recognized (Massenzio et al., 2023, 2024). The presence of a phreatic explosion crater and travertine domes suggests that hydrothermal activity was more intense in the past. At Piscinas Burbujeantes del Galán, acid–sulphate bubbling pools and geothermal fumaroles with temperatures of 80 and 87.7 °C, respectively, occur (Fig. 2F). Siliceous sinter deposits and fragments of the silicified Cerro Galán Ignimbrite were observed in the elevated topographic regions (Chiodi et al., 2024). Minerals such as kaolinite, hematite, boehmite, sulfates, sulfur, and others were identified around the bubbling pools (Massenzio et al., 2023, 2024).

The soils hosting the thermal emissions differ among the studied areas. At Aguas Calientes, the hot springs discharge through fluvial sediments forming terraced alluvial fans along the Aguas Calientes river. These deposits are poorly sorted and consist of alternating coarse and fine layers, with cross-lamination and planar lamination in the finer sandy levels; clasts are derived from ignimbrites, lavas, and the igneous-metamorphic basement. By contrast, the soils at La Colcha and Piscinas Burbujeantes mainly originate from the weathering of the Cerro Galán ignimbrite, forming terraced alluvial fans (Chiodi, 2015). Field observations during this study indicate that these deposits are also fine-grained and poorly consolidated.

2.2.1. Soil CO_2 diffuse degassing at CGC

Anomalously high CO_2 fluxes, up to 21.66 g m^{-2} d^{-1}, were measured at La Colcha and Aguas Calientes thermal sites, except for Piscinas Burbujeantes del Galán, where soil diffuse degassing is practically absent. Such high CO_2 fluxes were coupled with soil temperature anomalies, up to 35 °C. The log probability plot of the CO_2 fluxes showed three log-normal populations at La Colcha and two log-normal populations at Aguas Calientes (Massenzio et al., 2024). At La Colcha, the high-flux population was characterised by mean values of 18.63 g m^{-2} d^{-1}, whereas at Aguas Calientes, high-fluxes were characterised by mean values of 11.65 g m^{-2} d^{-1}. These high fluxes constituted 4 % and 10 % of the measured fluxes, respectively. The low-flux populations were defined by fluxes ranging from <0.01 to 2 g m^{-2} d^{-1}.

According to Massenzio et al. (2024), the high-flux populations originate from magmatic-hydrothermal sources, based on the spatial correlation between DDS and thermal anomalies. The low-flux populations were attributed to background CO_2 levels, mostly produced

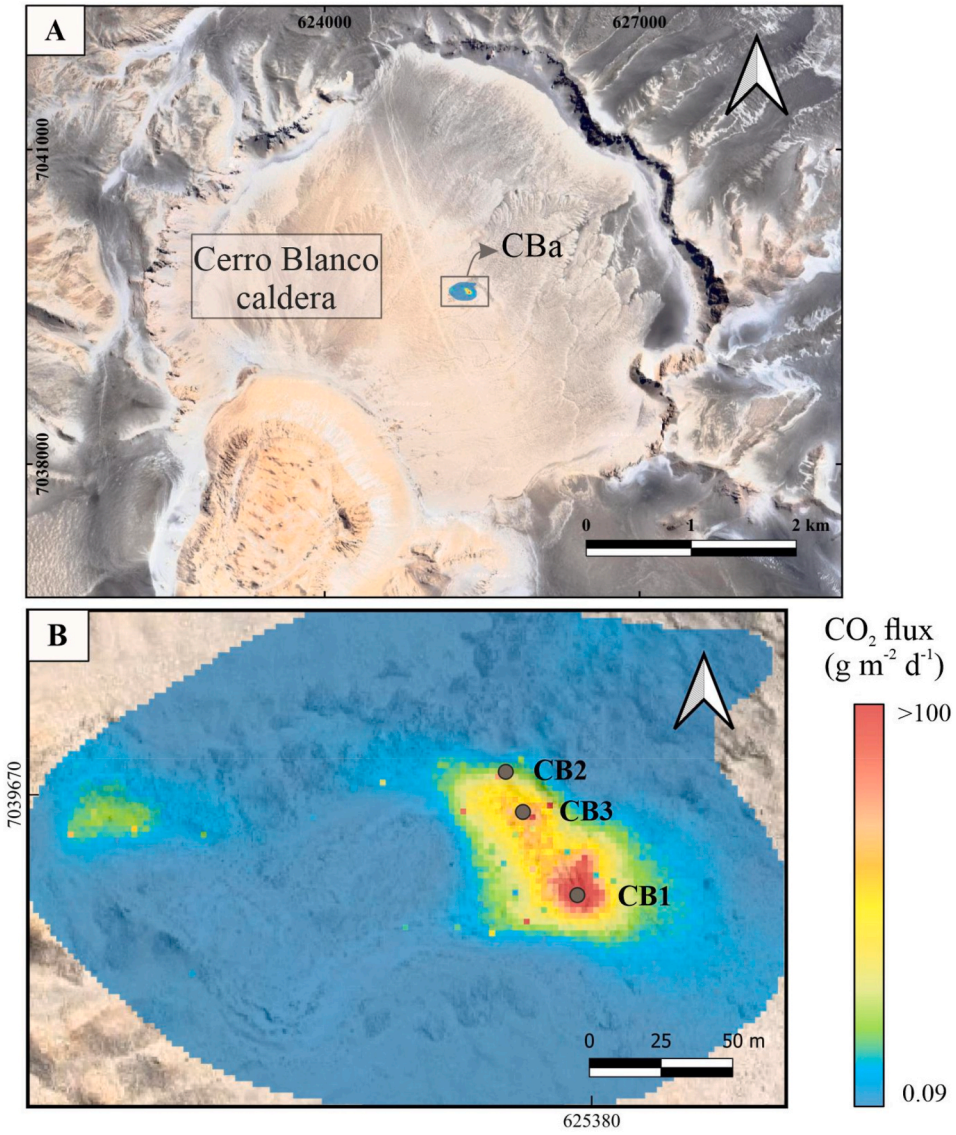

Fig. 3. A) Location of the diffuse degassing structure within the CBC. B) CO_2 flux map at CBa (Lamberti et al., 2021b). Grey points mark the soil gas sampling points from this work. Maps coordinates expressed in meters, UTM - WGS84, 19S.

within the soil.

The total diffuse CO_2 output at CGC was estimated at 201.35 kg d^{-1} ± 22.14, whereas the endogenous CO_2 outputs were 0.44 kg d^{-1} in La Colcha and 19.02 kg d^{-1} in Aguas Calientes (Massenzio et al., 2024). Low CO_2 output was attributed to partial dissolution of CO_2 in shallow water bodies combined with low soil permeability, which hinders upward gas transport (Massenzio et al., 2024).

3. Material and methods

Interstitial gas sampling from vertical profiles, three at CBC and ten at CGC each extending up to 40 cm depth, were carried out to analyze the concentration and carbon isotopic composition of CO_2 at various depths. At each gas sampling site, diffuse CO_2 flux and soil temperature were also measured (Table 1).

3.1. Soil CO_2 flux and temperature

Diffuse CO_2 flux (Φ) measurements were carried out according to the accumulation chamber method (Chiodini et al., 1998), using a West Systems portable flowmeter from GESVA - University of Buenos Aires. A 2.765×10^{-3} L chamber was placed on the ground, and the pump in the flowmeter continuously transferred gas from the chamber to a LICOR Li-820 infrared spectrometer, which is based on a Non-Dispersive Infrared (NDIR) technique and operates in the range of 0–20000 ppm of CO_2. After passing through the detector, the gas returns to the chamber. This minimises any disturbance to the gas flow. An Analog-Digital converter in the flowmeter allows flux results to be viewed on a mobile device using the Flux Manager software. The flowmeter was calibrated at the Argentine National Commission of Atomic Energy (CNEA) laboratories. The measurement uncertainty is around 10 % for CO_2 fluxes ranging from 10 to 10000 g m^{-2} d^{-1} (Chiodini et al., 1998), though this uncertainty may increase for lower fluxes (Carapezza and Granieri, 2004). Simultaneously with the ΦCO_2 measurements, soil temperature was measured at a depth of 10 cm suing a Hanna HI-935005 N digital thermometer with an accuracy of ±0.2 °C, and a thermocouple operating between −50 and 120 °C, with a resolution of 0.1 °C.

3.2. Sampling of soil gases

During a survey performed in November 2022 at the CBC and CGC,

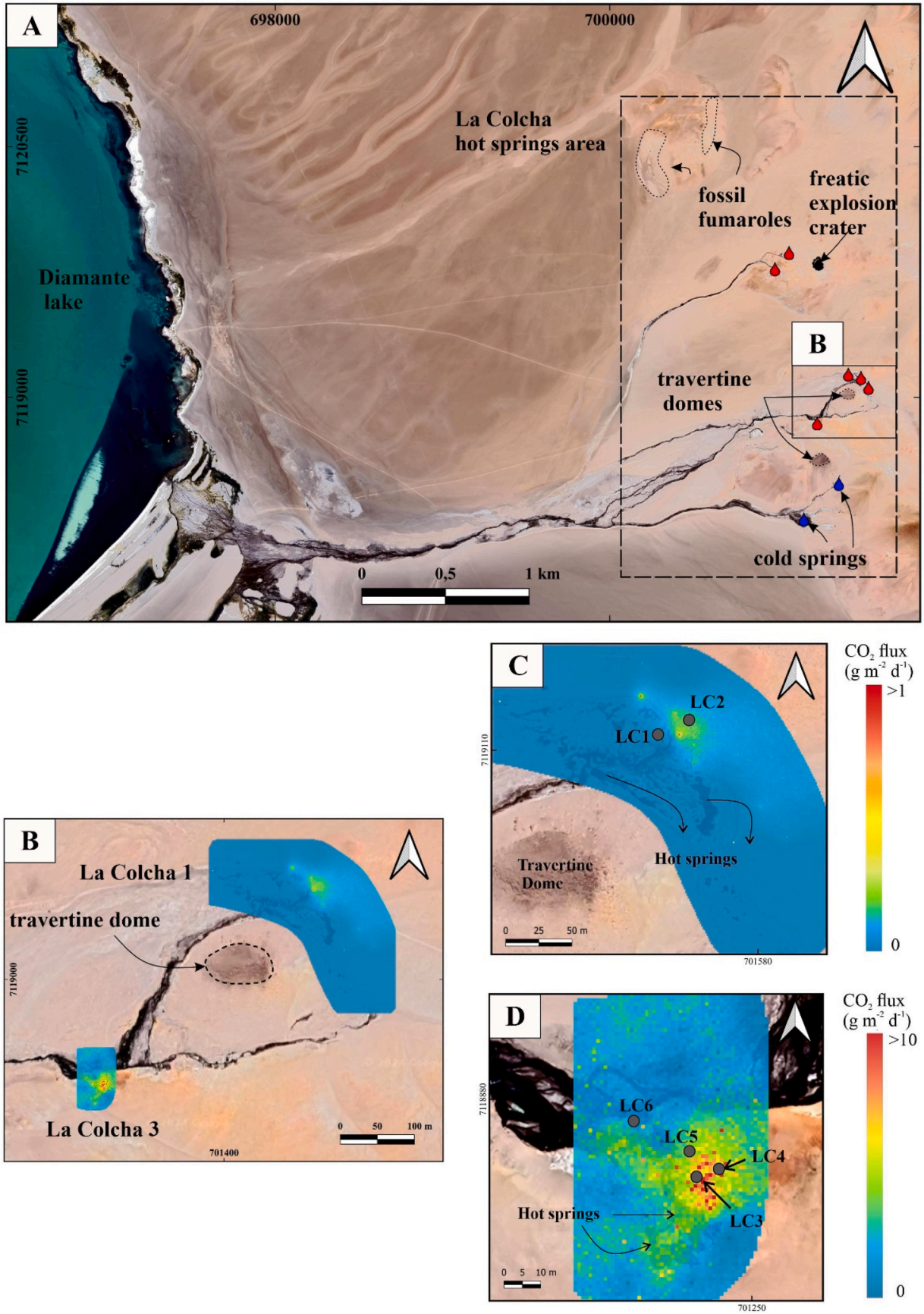

Fig. 4. A) Location of the diffuse degassing structures within the La Colcha thermal site. B) CO_2 flux maps at subsites within La Colcha (modified from Massenzio et al., 2024). C) CO_2 flux map at thermal site La Colcha 1 (Massenzio et al., 2024). D) CO_2 flux map at La Colcha 3 (Massenzio et al., 2024). Grey points mark the soil gas sampling points from this work (LC1, L2, L3, L4, L5, L6). Maps coordinates expressed in meters, UTM - WGS84, 19S.

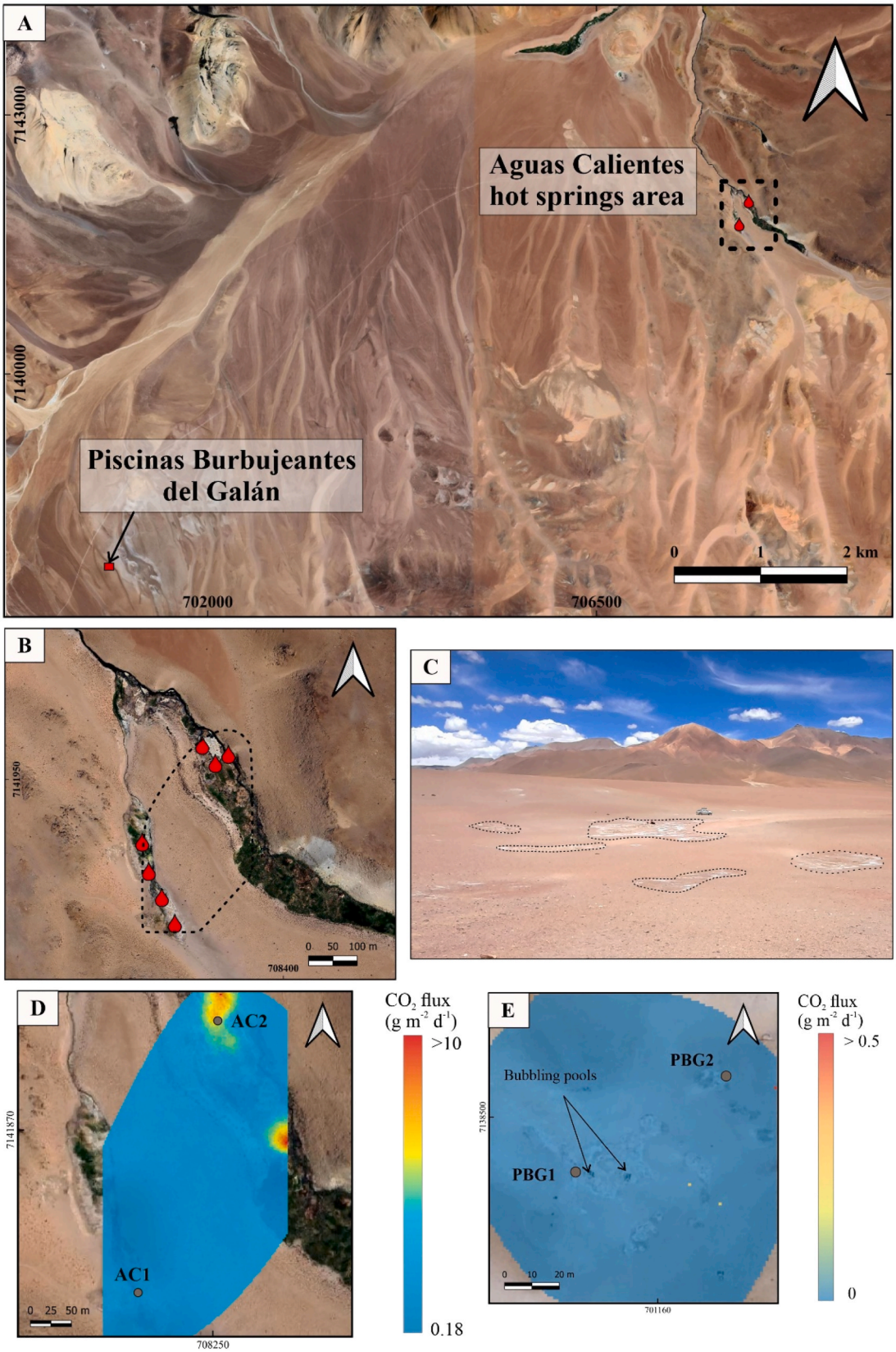

Fig. 5. A and B) Location of the Aguas Calientes and Piscinas Burbujeantes del Galán thermal site. B) Detailed view of the thermal site Aguas Calientes. C) View (toward W) of the Piscinas Burbujeantes del Galán thermal site. D) CO_2 flux map at thermal site Aguas Calientes (Massenzio et al., 2024) E) CO_2 flux map at Piscinas Burbujeantes del Galán thermal site (Massenzio et al., 2024). Grey points mark the soil gas sampling points from this work (AC1, AC2, PBG1 and PBG2). Maps coordinates expressed in meters, UTM - WGS84, 19S.

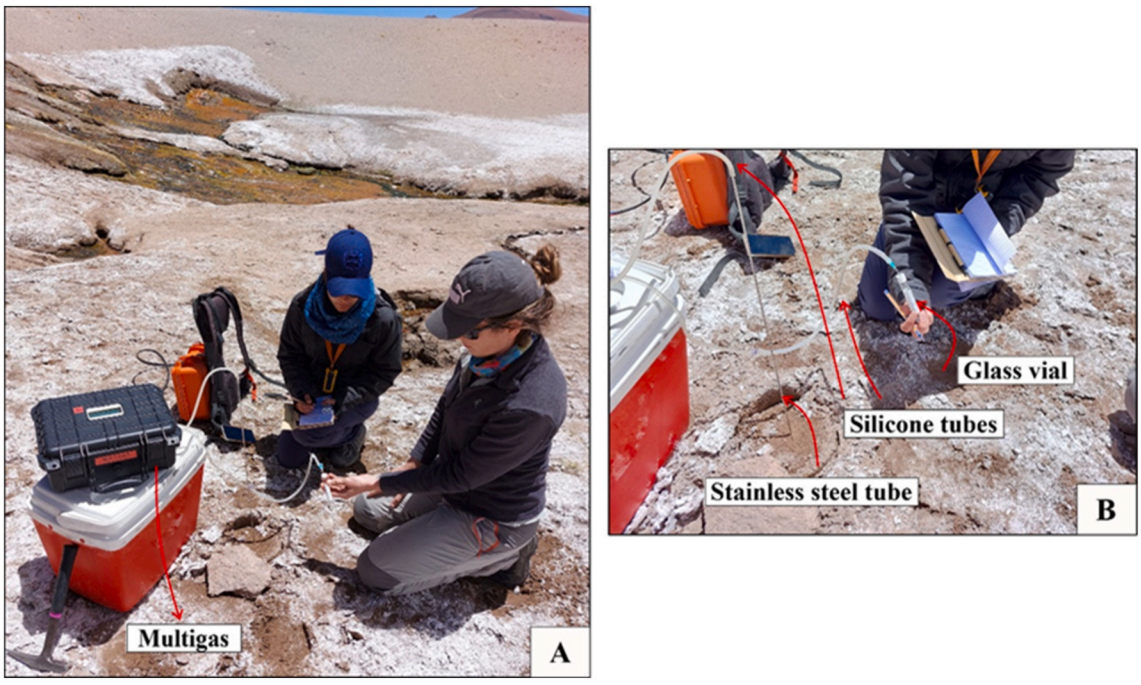

Fig. 6. A) Soil gas sampling at La Colcha. B) Details of the sampling elements.

we collected 35 samples of interstitial soil gases, as follows: at CBC, 8 samples along three vertical profiles within CBa (CB1, CB2 and CB3, Fig. 3A and B), and at CGC, 27 soil gas samples from 10 vertical profiles (Fig. 4A and B and 5A,B,C). Among the latter, 6 profiles were carried out at La Colcha thermal site (LC1, LC2, LC3, LC4, LC5, LC6; Fig. 4C and D), 2 profiles at Aguas Calientes thermal site (AC1, AC2; Fig. 5D), and 2 profiles at Piscinas Burbujeantes del Galán (PBG1, PBG2; Fig. 5E). Soil gas samples were collected by inserting a stainless-steel tube with an inner diameter of 0.4 mm, at 10, 20, 30, and 40 cm depths (Fig. 6), except in some sites where soil conditions did not allow us to reach the 30/40 cm depths. We performed the sampling sequentially from the surface downward, in order to minimize disturbance during perforation. All samples belonging to the same profile were taken from the same hole (Table 1). The different profiles corresponded to independent holes located a few meters apart (Fig. 4C and D and 5D,E).

We connected the stainless-steel tube to a Multigas gas analyzer developed by the ICES group from the CNEA (Argentina). This instrument was equipped with three gas sensors: (i) a non-dispersive infrared Gascard NG CO_2 sensor (Edinburgh Sensors), operating in the range of 0–5000 ppm with an accuracy of 2 % and a resolution of 0.8 ppmv; (ii) an electrochemical Alphasense H_2S sensor, with a measuring range of 0–50 ppm, accuracy of 0.1 ppm, and resolution of 0.048 ppm; and (iii) an electrochemical Alphasense SO_2 sensor, with a measuring range of 0–200 ppm, accuracy of 0.1 ppm, and resolution of 0.19 ppm. The system also incorporated a flux pump (1 L/min), ensuring a constant gas flow through the sensors. At the outlet vent of the CO_2 detector, we connected a silicone tube to a 12 mL glass vial equipped with a pierceable rubber septum (Labco Exetainer®), to collect gas samples for isotopic analyses (Fig. 6B).

We analyzed the $\delta^{13}C$–CO_2 values (expressed as ‰ vs. V-PDB) by Cavity Ring-Down Spectroscopy (CRDS) using a Picarro G2201-i Analyzer at the Fluid Geochemistry Laboratory, Department of Earth Sciences, University of Florence (Italy). The instrument inlet line was equipped with Drierite and copper traps to remove water vapour and H_2S. The analytical error was ±0.16 ‰ (Venturi et al., 2019; Tassi et al., 2022).

4. Results

4.1. Soil CO_2 flux and soil temperature

The three profiles at CBC (Fig. 3B) were conducted within DDS areas and showed CO_2 fluxes between 22.5 and 39.9 g m^{-2} d^{-1}. Soil temperatures were within a relatively narrow range (36.6–48.2 °C; Table 1). These profiles were only collected within DDS areas due to time constraints during the field survey.

The ten profiles surveyed at CGC were conducted both within and outside DDS areas (Figs. 4 and 5). CO_2 fluxes measured at the profile points were low (from 0.78 to 9.1 g m^{-2} d^{-1}) and were associated with moderate to high soil temperatures (from ~21 to 61 °C).

Soil CO_2 flux measurements were always conducted on the dry soil surface before inserting the sampling tube, reflecting the actual conditions at the measurement point.

4.2. CO_2 concentration and carbon isotopic composition of soil CO_2 at CBC

The concentrations of CO_2 in interstitial soil gases at CBC ranged from 540 to >5000 ppm, while the $\delta^{13}C$-CO_2 values varied between −15.4 and −4.9 ‰ vs. V-PDB (Table 1).

Soil gas composition along the three vertical profiles (Table 1) showed different trends at increasing depth:

i) The CB1 profile is characterized by an increase in both CO_2 concentration and $\delta^{13}C$-CO_2 (540–850 ppm and −15.4 to −11.7 ‰ vs. V-PDB respectively).
ii) The CB2 profile shows concentrations >5000 ppm at 10 and 20 cm depth, with $\delta^{13}C$-CO_2 values of −4.9 to −5.6 ‰ vs. V-PDB, respectively.
iii) The CB3 profile shows a sharp decrease with depth in CO_2 concentration (from >5000 to 780 ppm), accompanied by an abrupt depletion of $\delta^{13}C$-CO_2 from −5.2 to −14.3 ‰ vs. V-PDB.

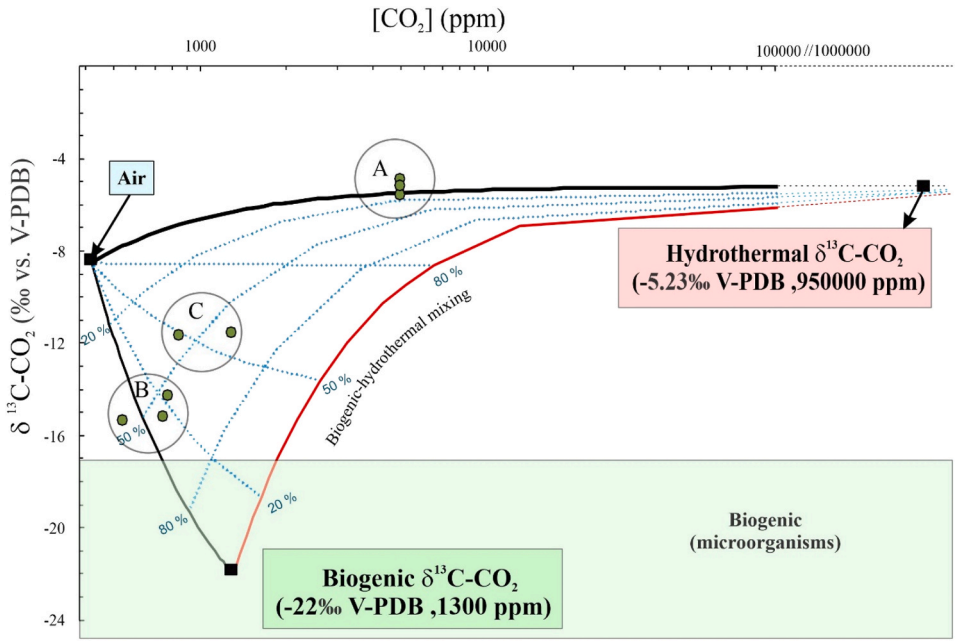

Fig. 7. Plot of δ^{13}C-CO_2 values against CO_2 concentration for soil gas samples at CBC. CO_2 concentrations (green dots) are evaluated according to a mixing process of three components (hydrothermal-air-biogenic). Solid black lines and the red line represent mixing paths between principal endmembers. The red line (Biogenic - hydrothermal mixing) joins the hydrothermal endmember at δ^{13}C-CO_2 -5.23 ‰ vs. V-PDB and a CO_2 concentration of 950000 ppm. Group **A** includes data points where the CO_2 is predominantly from a hydrothermal source. Group **B** includes data points with a higher biogenic CO_2 contribution, and Group **C** includes data points that fall within the mixing field with contribution from the three sources.

4.3. CO_2 concentration and carbon isotopic composition of soil CO_2 at CGC

The CO_2 concentration ranged from 370 to >5000 ppm and the δ^{13}C-CO_2 values ranged from −21.3 to −5.2 ‰ vs. V-PDB (Table 1). Samples collected from the DDS profiles at both La Colcha and Aguas Calientes sites, with CO_2 concentrations exceeding 5000 ppm, exhibit carbon isotopic compositions of −5.2 ‰ (LC4) and −6.5 ‰ vs. V-PDB (AC1), respectively ($\Delta = -1.3$ ‰, $\bar{x} = -5.83$ ‰ vs. V-PDB). At La Colcha, we also obtained a sample within a DDS with CO_2 concentrations below 5000 ppm but similar isotopic values (−5.8 ‰ vs. V-PDB at 1000 ppm, LC5; Table 1 and Fig. 8).

The CO_2 composition of soil interstitial gases along the ten vertical profiles at CGC can be described as follows:

i) The LC1 profile was characterised by CO_2 concentrations from 400 to 500 ppm, whereas the δ^{13}C-CO_2 values ranged from −18.8 to −19.6 ‰ vs. V-PDB. Samples in this profile could only be taken up to a depth of 20 cm due to soil characteristics that prevented deeper sampling.
ii) The CO_2 concentrations and δ^{13}C-CO_2 values in profiles LC2, LC6, and AC2 showed only minor variations. In profile LC2, the CO_2 concentration slightly increased from 600 to 700 ppm between 10 and 30 cm, and the δ^{13}C-CO_2 values were −17.6 ‰ at 10 cm, −17.8 ‰ at 20 cm, and −11.4 ‰ at 30 cm. In profile LC6, the CO_2 concentration was 600 ppm at both 10 cm and 30 cm, while it increased to 650 ppm at 20 cm. The δ^{13}C-CO_2 values were −15.7 ‰ at 10 cm, −14.8 ‰ vs. V-PDB at 20 cm, and −15.1 ‰ vs. V-PDB at 30 cm. In profile AC2, the CO_2 concentration was 600 ppm at 10 cm and 700 ppm at both 20 cm and 30 cm. The δ^{13}C-CO_2 values were −17.6 ‰ vs. V-PDB at 10 cm, −15.6 ‰ vs. V-PDB at 20 cm, and −15.9 ‰ vs. V-PDB at 30 cm.
iii) The LC3 and PBG1 profiles showed an increase in CO_2 concentration with depth. The concentration ranged from 370 to 400 ppm to approximately 600–650 ppm. The δ^{13}C-CO_2 values showed an increase from 10 cm to 40 cm depth: from −19.7 ‰ to −13.2 ‰ vs. V-PDB at LC3 and from −21.3 ‰ vs. V-PDB to −15.4 ‰ vs. V-PDB at PBG1.
iv) Only one sample was collected at 10 cm in the LC4 site, which showed a concentration of >5000 ppm and a δ^{13}C-CO_2 value of −5.2 ‰ vs. V-PDB. Further sampling was not possible due to water soil saturation.
v) In the LC5 and AC1 profiles, CO_2 concentration decreases with depth from over 5000/1000 ppm to 600/700 ppm, while in PBG2, the concentration showed less variation, decreasing only from 710 to 630 ppm. The δ^{13}C-CO_2 in the LC5 and AC1 profiles becomes lighter, from −5.8 and −6.5 ‰ vs. V-PDB to ~ −14 and −13 ‰ vs. V-PDB, respectively. In PBG2, the variation was smaller, from −13.3 to −18.8 ‰ vs. V-PDB.
vi) The CO_2 concentration and δ^{13}C-CO_2 values in the LC6 and AC2 profiles showed only minor variation. At LC6, the CO_2 concentration was 600 ppm at both 10 cm and 30 cm, but increased to 650 ppm at 20 cm. The δ^{13}C-CO_2 values were −15.7 ‰ at 10 cm, −14.8 ‰ vs. V-PDB at 20 cm, and −15.1 ‰ vs. V-PDB at 30 cm. At AC2, the CO_2 concentration was 600 ppm at 10 cm and increased to 700 ppm at both 20 cm and 30 cm. The δ^{13}C-CO_2 values were −17.6 ‰ vs. V-PDB at 10 cm, −15.6 ‰ vs. V-PDB at 20 cm, and −15.9 ‰ vs. V-PDB at 30 cm.

4.4. Three-component mixing model

We processed the CO_2 concentration and δ^{13}C-CO_2 data following the three-component mixing model described by Lucic et al. (2015) and Di Martino et al. (2016), in order to estimate the relative contribution of hydrothermal, atmospheric, and biogenic sources to soil gas composition. To calculate three-component mixing, we used the following equations:

$$1 = f_H + f_A + f_B \quad (1)$$

$$\delta^{13}C_{obs} = f_H(\delta^{13}C_H) + f_A(\delta^{13}C_A) + f_B(\delta^{13}C_B) \quad (2)$$

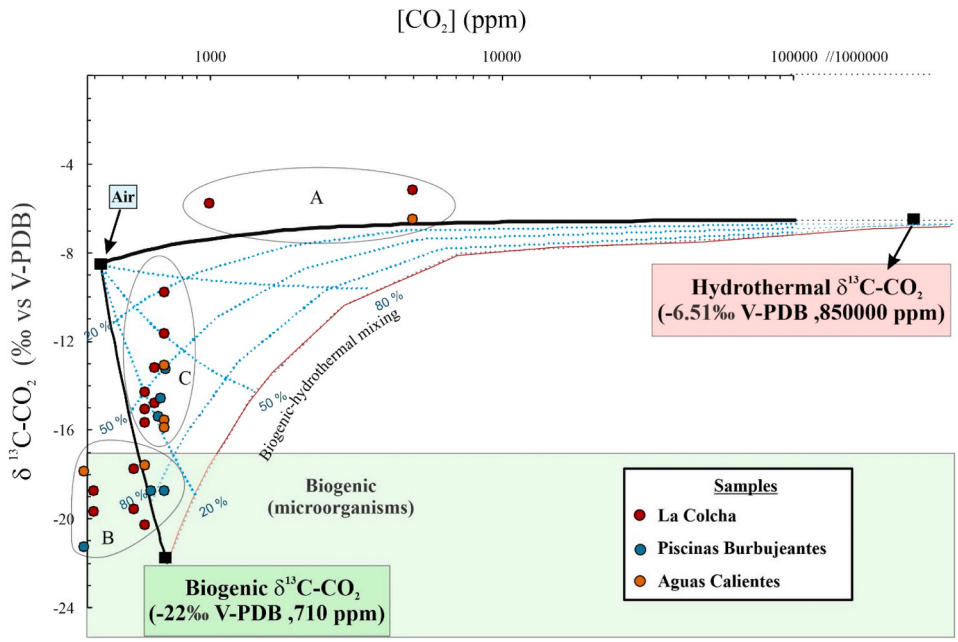

Fig. 8. Plot of δ^{13}C-CO_2 values against CO_2 concentration for soil gas samples at CGC. The CO_2 is evaluated according to a mixing process of three components (hydrothermal-air-biogenic). Solid black lines and the red line represent mixing paths between principal end-members. The red line (Biogenic - hydrothermal mixing) joins the hydrothermal zone at 850000 ppm. Group **A** includes data points where the CO_2 is predominantly from a hydrothermal source. Group **B** includes data points where the CO_2 is mainly from a biogenic source, and Group **C** includes data points within the mixing field between the three sources.

$$\frac{1}{CO_2 obs} = \frac{f_H}{CO_{2H}} + \frac{f_A}{CO_{2A}} + \frac{f_B}{CO_{2B}} \quad (3)$$

where the subscripts H, A, and B correspond to hydrothermal, atmospheric, and biogenic end-members, respectively. The parameter f represents the relative fraction for each source, δ^{13}C represents the isotopic composition in ‰, and CO_2 corresponds to the concentration of gas in vol %.

The CO_2 concentrations of each end-member are reported in ppm Figs. 7 and 8 for clarity; for the mixing calculations, these values were converted to vol% (Supplementary Material 1). The end-member values used in this study are:

- Cerro Blanco caldera: hydrothermal $\delta^{13}C_H = -5.23$ ‰ and $CO_{2\,H} = 950000$ ppm, atmospheric $\delta^{13}C_A = -8.5$ ‰ and $CO_{2\,A} = 418$ ppm, and biogenic $\delta^{13}C_B = -22.0$ ‰ and $CO_{2\,B} = 1300$ ppm.
- Cerro Galán caldera: hydrothermal $\delta^{13}C_H = -6.51$ ‰ and $CO_{2\,H} = 850000$ ppm, atmospheric $\delta^{13}C_A = -8.5$ ‰ and $CO_{2\,A} = 418$ ppm, and biogenic $\delta^{13}C_B = -22$ ‰ and $CO_{2\,B} = 540$ ppm.

Nearly all soil gas samples could be explained as mixtures of these three components. The resulting relative contributions (f_H, f_A, f_B) were then calculated for all sampling points (Supplementary material 1). Samples that did not fit the mixing model (i.e., yielding non-physical results such as negative fractions) were not converted to relative percentages and are indicated with "–". The rationale for selecting the end-member values for each caldera is further discussed in Section 5.

5. Discussion

5.1. Origin of soil CO_2 at CBC

The three-component mixing model was constructed using CO_2 concentrations and δ^{13}C-CO_2 values from regional endmembers of the three sources, based on previous studies conducted in and around the area (Samec et al., 2015; Chiodi et al., 2019; Raegan et al., 2023).

(1) The CO_2 of hydrothermal origin presents a concentration of 950000 ppm and a δ^{13}C-CO_2 of −5.23 ‰ vs. V-PDB, measured in fumarolic gases from the CBa hydrothermal site (Chiodi et al., 2019). This value ranges in the magmatic CO_2 values for the Central Volcanic Zone from −12.0 ‰ to −1.2 ‰ vs. V-PDB (Barry et al., 2022).

(2) The average δ^{13}C-CO_2 value for biogenic sources related to Puna vegetation is −25.4 ‰ vs. V-PDB (Samec et al., 2015), consistent with the typical range for C3 plants (−35 to −20 ‰) that dominate temperate and high altitude environments, such as those in the southern Andes (Tieszen, 1991; Dawson et al., 2002; Panarello and Fernández, 2002). In the CBC, the sparse herbaceous steppe vegetation is dominated by *Festuca* spp. and uses the C3 pathway of photosynthesis, but is outside the hydrothermal zone (Fig. 1B). Within the hydrothermal zone, where vegetation is absent, isotopic values likely reflect microbial respiration. While specific studies for the CBC are lacking, chemolithoautotrophic microorganisms have been identified in similar geothermal systems in the Central Volcanic Zone of Argentina, such as Tocomar and CGC (Raegan et al., 2023). Though isotopic data are unavailable for Tocomar and CGC, chemolithoautotrophic communities in hydrothermal deposits, such as those at Solfatara (Glamoclija et al., 2004), show ^{13}C isotopic signatures between −27.39 and −17.09 ‰ vs. V-PDB. Based on this information, we select δ^{13}C-CO_2 = −22 ‰ vs. V-PDB (the mean value of the chemolithoautotrophic microorganisms' range, as the endmember for soil respiration (biogenic CO_2), as it closely approximates the expected carbon isotope composition of CO_2 in the soil gases at CBC. Excluding concentrations above 5000 ppm, which are associated with δ^{13}C-CO_2 values indicative of a hydrothermal origin, the highest CO_2 concentration measured at CBC (1300 ppm) is considered part of the soil respiration (biogenic CO_2) endmember. The selection of these values follows the same criteria used in previous studies (Lucic et al., 2015; Di Martino et al., 2016, 2020). They selected the highest CO_2 concentrations measured in the field (Vulcano), considering only those associated with the lowest δ^{13}C-CO_2 values, based on the assumption

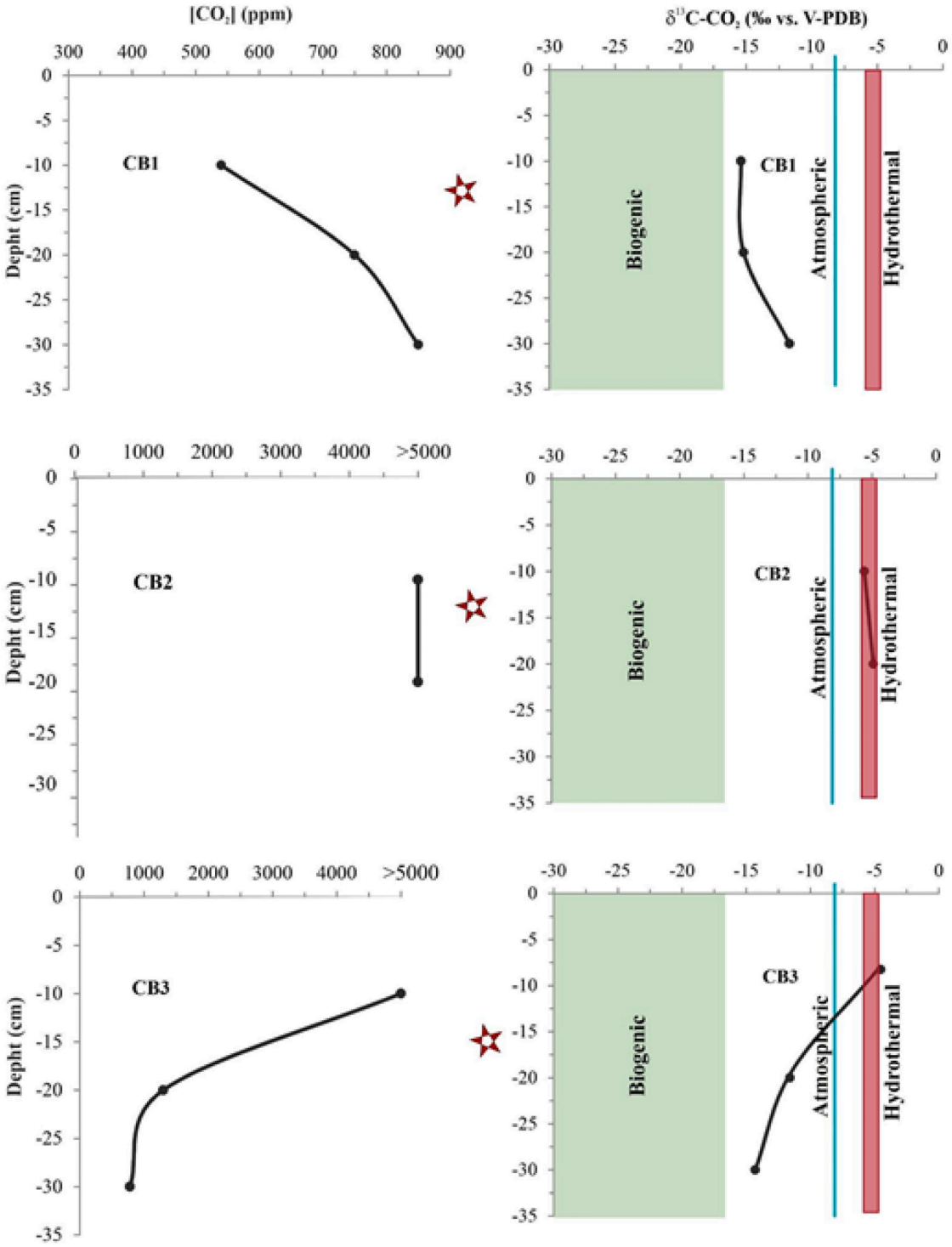

Fig. 9. Vertical profiles of soil CO_2 concentration and $\delta^{13}C$-CO_2 values at CBC (see location of CB1, CB2 and CB3 in Fig. 3b). The green shaded box corresponds to the biogenic $\delta^{13}C$-CO_2 range between -30 and -17 ‰ vs. V-PDB. The light blue corresponds to the $\delta^{13}C$-CO_2 atmospheric value, -8.5 ‰ vs. V-PDB. The red shaded box corresponds to the hydrothermal $\delta^{13}C$-CO_2 values ranging from -5.6 and -4.9 ‰ vs. V-PDB. The red stars mark the profiles conducted on a diffuse degassing structure. The information provided by the colour references is detailed in subsection 5.1.

that CO_2 produced by soil respiration is more ^{13}C-depleted than hydrothermal.

(3) The atmospheric endmember is defined by CO_2 concentration of 400 ppm and isotopic composition of $\delta^{13}C$-$CO_2 = -8.5$ ‰ vs. V-PDB, according to Pieber et al. (2021).

The CO_2 concentration and $\delta^{13}C$-CO_2 values of the hydrothermal, biogenic and atmospheric endmembers of the CBC were used to obtain the three binary mixing curves shown in Fig. 7. From the scatter data in this mixed model diagram, three main groups (A, B and C) at CBC are recognized. Group A consists of three samples with the highest contribution from the hydrothermal source ($\delta^{13}C$-CO_2 range from -5.6 ‰ to -4.9 ‰ vs. V-PDB, and >5000 ppm CO_2). In one of these samples, the mixing model indicates a hydrothermal contribution clearly >90 %.

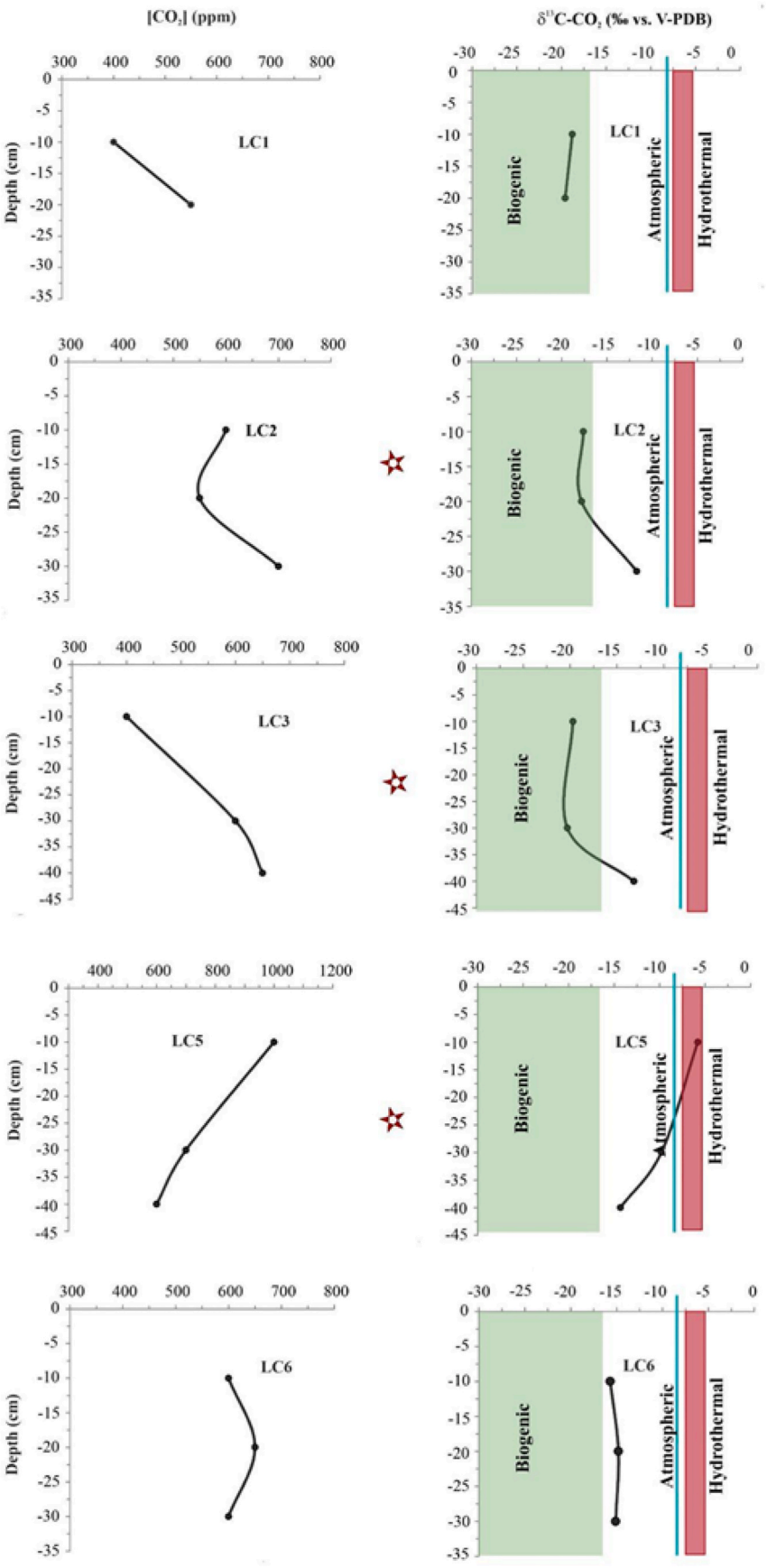

(caption on next page)

Fig. 10. Vertical profiles of soil CO_2 concentration and $\delta^{13}C$-CO_2 values at La Colcha (see location of LC1,6 profiles in Fig. 4). The green shaded box corresponds to the biogenic $\delta^{13}C$-CO_2 range between −30 and −17 ‰ vs. V-PDB. The light blue corresponds to the atmospheric value, $\delta^{13}C$-CO_2 -8.5 ‰ vs. V-PDB. The red shaded box corresponds to the hydrothermal $\delta^{13}C$-CO_2 values ranging from −7.5 and −5.2 ‰ vs. V-PDB. The red stars mark the profiles conducted on a diffuse degassing structure. The information provided by the colour references is detailed in subsection 5.2.

However, two of these samples could not be reproduced by the simple three-component mixing model, as it returned negative contributions for one of the end-members. This suggests two possible explanations: (i) the selected end-members, particularly the hydrothermal and biogenic ones, may not fully represent the local variability, or (ii) secondary processes induce isotopic fractionation. Among the latter, advective–diffusive transport through porous media can preferentially release lighter ^{12}C to the atmosphere while retaining heavier ^{13}C in the soil, a process particularly common under low flux conditions when gas transport is dominated by diffusion (Capasso et al., 2001; Camarda et al., 2007). This interpretation is consistent with our dataset, where all sampling points presents low CO_2 fluxes (Table 1). Another possibility is the partial dissolution of CO_2 in shallow waters or soil pore waters (Ma et al., 2013, 2015, and references therein). In arid environments, abiotic processes such as carbonate dissolution/precipitation and changes in CO_2 solubility within soil water films can also influence CO_2 fluxes. Specifically, increasing temperature decreases CO_2 solubility, promoting the exsolution of dissolved CO_2 back into the gaseous phase. This mechanism leaves the soil CO_2 enriched in ^{13}C, resulting in more positive $\delta^{13}C$ values (Shanhun et al., 2012). In agreement with this, our measurements indicate relatively high soil temperatures at CBC, which would enhance CO_2 exsolution processes and thus contribute to the observed positive $\delta^{13}C$ shifts. We consider the first explanation more likely, because, as previously noted, magmatic CO_2 values in this region display a wide compositional range (−12 to −1.2 ‰ vs. V-PDB, Barry et al., 2022). This broad isotopic spectrum suggests that a single fixed end-member value may not adequately capture the natural variability of the hydrothermal source, and thus a range of magmatic compositions should be considered when interpreting the mixing model. Similarly, the biogenic end-member may also be poorly constrained, since no $\delta^{13}C$-CO_2 values from vegetation or microbial activity have yet been reported for the caldera, as previously noted.

Group B includes soil gas samples in which CO_2 is mainly of a shallow biogenic source ($\delta^{13}C$-CO_2 range from −15.4 ‰ to −14.3 ‰ vs. V-PDB, and <800 ppm CO_2). On average, the three-component mixing model indicates contributions of 12.0 % hydrothermal, 38.8 % atmospheric, and 49.2 % biogenic CO_2, highlighting the predominance of the biogenic source while also reflecting significant atmospheric mixing.

Group C includes soil gas samples characterized by a more balanced mixture of the three sources, with average contributions of 37.4 % hydrothermal, 30.2 % atmospheric, and 32.4 % biogenic CO_2. Compared to Group B, the main difference is the increase in the hydrothermal contribution, highlighting the stronger influence of deep magmatic-hydrothermal fluids.

5.2. Origin of soil CO_2 at CGC

For the purpose of our three-component mixing model at CGC, the local hydrothermal and biogenic $\delta^{13}C$-CO_2 endmembers were defined according to previous works at CGC (Raegan et al., 2023; Chiodi et al., 2024; Massenzio et al., 2024):

(1) The $\delta^{13}C$-CO_2 value of −6.51 ‰ vs. V-PDB was defined as the hydrothermal endmember, gases emitted from the bubbling pools at the La Colcha thermal site (Barry et al., 2022; Chiodi et al., 2024). This value was selected as a reference because the fluids discharged at this site are representative of the deep Na^+-Cl^- hydrothermal aquifer (Chiodi et al., 2024).

(2) The biogenic endmember $\delta^{13}C$-CO_2 was the same as that selected for CBC (−22 ‰ vs. V-PDB); however, in this case, the highest CO_2 concentration measured—excluding values above 1000 ppm—was lower, at 710 ppm. This selected endmember value is within the isotopic range of chemolithoautotrophic microbial communities (−27.39 to −17.09 ‰), as reported by Glamoclija et al. (2004) in the Solfatara hydrothermal deposits. The presence of such communities at CGC is supported by Raegan et al. (2023), who identified chemolithoautotrophs in all three hydrothermal sites of the caldera. These microorganisms use CO_2 to synthesize organic matter, deriving energy from redox reactions that promote the formation of biominerals such as elemental sulfur, sulphides, sulphates, and iron oxides/hydroxides (Stetter, 2006; Glamoclija et al., 2004). Many of these minerals were also identified at Piscinas Burbujeantes (Massenzio et al., 2024), supporting the presence of similar microbial processes. Importantly, Raegan et al. (2023) indicated that these microbial communities survive by recycling organic matter derived from their own necromass. This organic substrate, which accumulates in the soil, likely acts as the source of biogenic CO_2 detected in diffuse soil emissions. Therefore, the selected $\delta^{13}C$-CO_2 value (−22 ‰) reasonably represents this biogenic contribution within the context of CGC.

(3) The third source, the atmosphere, maintains the aforementioned values of 400 ppm of CO_2 concentration and the isotopic composition of $\delta^{13}C$-CO_2 = −8.5 ‰ vs. V-PDB (Pieber et al., 2021).

As in CBC, the three endmembers were used to obtain three binary trend mixing curves reported in the $\delta^{13}C$-CO_2 vs. CO_2 concentration graph (Fig. 8). The data plotted show a dispersion ranging from a strong hydrothermal signature with higher CO_2 concentrations and $\delta^{13}C$-CO_2 values, to more depleted values, indicating a predominant contribution from the endmembers characterised by lower CO_2 concentrations and isotopically light CO_2.

As with CBC, the scatter data at CGC were discriminated into three groups (Fig. 8). Group A presents the highest contribution from the hydrothermal source. These samples were collected from the two sites where clear degassing structures are present (Figs. 4 and 5), highlighting a spatial correlation between surface degassing features and a strong hydrothermal signature. In contrast, at Piscinas Burbujeantes, no such structures were observed (Fig. 5E), and the isotopic signature also does not indicate a dominant hydrothermal contribution. One of the three Group A samples shows a lower CO_2 concentration (~1000 ppm), likely due to greater mixing with atmospheric CO_2. The samples fall outside the model predictions. The interpretation for this group follows the same reasoning as for Group A at CBC.

Group B consists of samples in which CO_2 is predominantly biogenic in origin (average ~74 %). Only three data points fall within the theoretical mixing field, plotting close to the atmospheric–biogenic mixing line. All samples deviate from the biogenic–hydrothermal trajectory. The absence of samples along this line can be explained by the extremely arid conditions of the study sites, where scarce vegetation results in lower rates of biogenic CO_2 production. This interpretation is supported by the lower CO_2 concentration values observed at Piscinas Burbujeantes del Galán and La Colcha (~400 ppm, Table 1), both sites where vegetation is absent. This supports the use of a biogenic endmember associated with microbial activity, rather than one derived from wetlands, as the more appropriate option for this setting.

Group C includes data that plot within the mixing field with contributions from all three end-members, with averaged proportions of 45.5 % biogenic, 17.8 % hydrothermal, and 36.6 % atmospheric. This

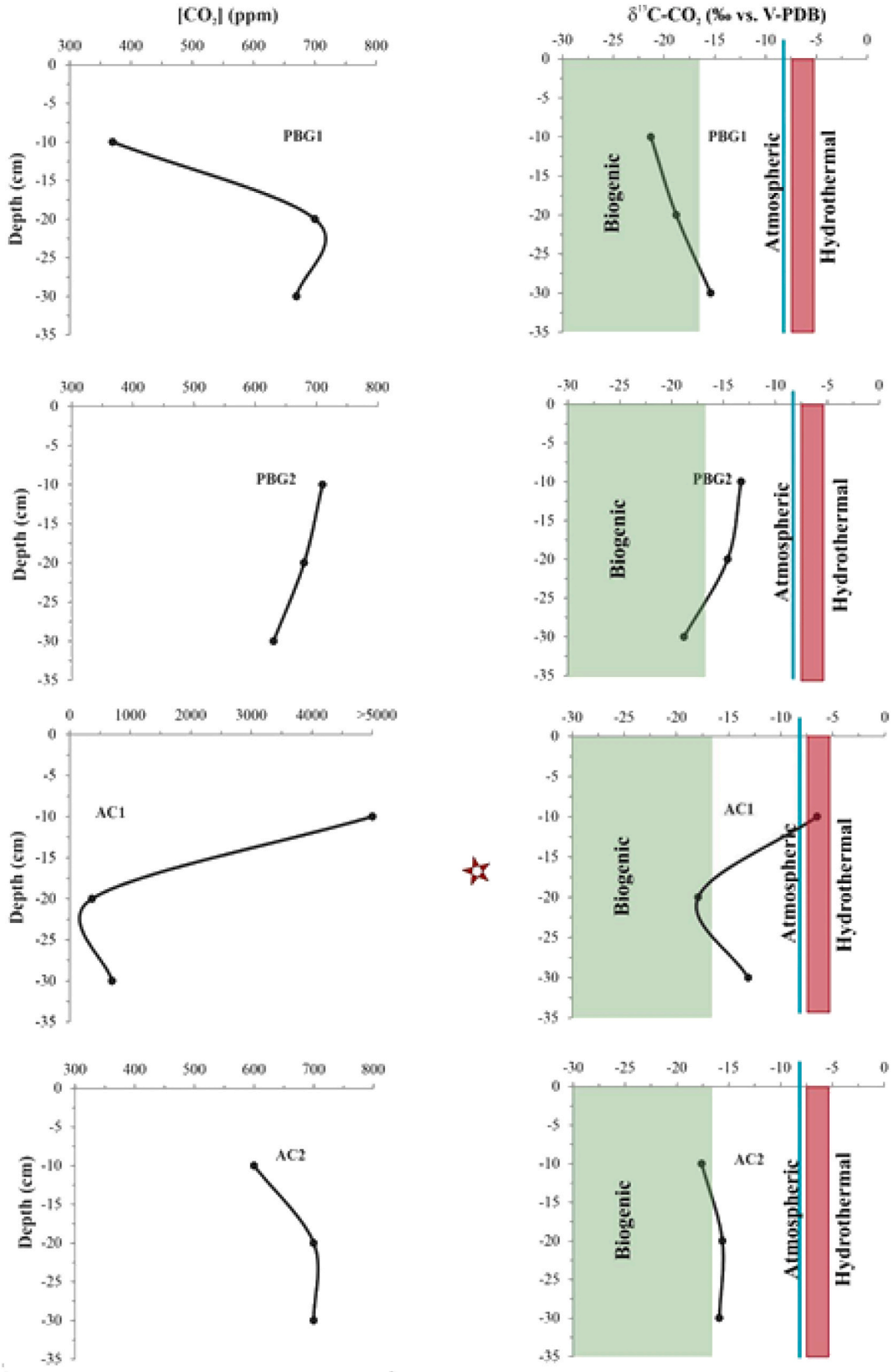

Fig. 11. Depth profiles of soil CO_2 concentration and $\delta^{13}C$-CO_2 values at Aguas Calientes (AC) y Piscinas Burbujeantes del Galán (PBG). See location of AC1,2 and PBG1,2 profiles in Fig. 5. The green shaded box corresponds to the biogenic $\delta^{13}C$-CO_2 range between −30 and −17 ‰ vs. V-PDB. The light blue corresponds to the atmospheric value, $\delta^{13}C$-CO_2 -8.5 ‰ vs. V-PDB. The red shaded box corresponds to the hydrothermal $\delta^{13}C$-CO_2 values ranging from −7.5 and −5.2 ‰ vs. V-PDB. The red stars mark that the profiles were carried out on a diffuse degassing structure. The information provided by the colour references is detailed in subsection 5.2.

suggests that the observed CO_2 reflects a combined influence of microbial activity, magmatic-hydrothermal input, and air. Samples from all three sites fall within this group, and interestingly, at Piscinas Burbujeantes del Galán a minor hydrothermal contribution is still detected in the soil, despite the absence of measurable diffuse CO_2 emissions at the surface.

While the three-component mixing model captures the main trends at CGC, some samples from both La Colcha and Aguas Calientes fall outside the model predictions. In these sites, where carbonate minerals are known to occur (Massenzio et al., 2024), secondary processes such as carbonate precipitation or dissolution may locally modify the isotopic signal, respectively depleting or enriching the CO_2 in ^{13}C (Barry et al., 2013; Vignoni et al., 2024). In addition, we cannot rule out that microbial activity itself may act as a secondary process locally modifying the $\delta^{13}C\text{-}CO_2$ signal in the three sites, potentially leading to either an enrichment or a depletion in ^{13}C (Blair et al., 1985; Wang et al., 2017). Nevertheless, since no additional sampling for verification was carried out, the reported $\delta^{13}C$ values could also reflect instrumental error or sample contamination. In addition, the uncertainties of the method—particularly high at low CO_2 efflux values—may partly account for the observed dispersion in the $\delta^{13}C\text{-}CO_2$ data (Chiodini et al., 2008).

5.3. Variability of CO_2 concentration and $\delta^{13}C\text{-}CO_2$ in vertical profiles at CGC and CBC

The vertical profiles analyzed in both the CBC and CGC areas (Figs. 9–11) exhibit significant deviations from the theoretical CO_2 concentration and $\delta^{13}C\text{-}CO_2$ distribution patterns described in previous studies. Camarda et al. (2007) and Federico et al. (2010) reported that, in vertical profiles of volcanic-hydrothermal soils, CO_2 concentrations generally increase with depth, while $\delta^{13}C\text{-}CO_2$ values progressively approach those of the deep source, moving away from the atmospheric compositions typically observed in the uppermost soil layer (<10 cm).

In the CBC area, the CB2 profile (Fig. 9), which includes samples from 10 cm to 20 cm depths, both CO_2 concentration (>5000 ppm) and $\delta^{13}C\text{-}CO_2$ values (−4.9 to −5.6 ‰ vs. V-PDB) remained relatively constant. This profile reflects the hydrothermal characteristics, indicating a stable contribution from the hydrothermal source. Meanwhile, the CB1 and CB3 profiles (Fig. 9) display direct correlations between CO_2 concentration and $\delta^{13}C\text{-}CO_2$. In the CB1 profile, both CO_2 concentration and $\delta^{13}C\text{-}CO_2$ increased with depth, while in the CB3 profile, both variables decreased with depth (Fig. 9).

Similarly, in the CGC area, most profiles also exhibit a direct correlation between CO_2 and $\delta^{13}C\text{-}CO_2$, though with varying trends. Profiles such as LC2, LC3 (Fig. 10); PBG1, and AC2 (Fig. 11) show increasing CO_2 concentrations and $\delta^{13}C\text{-}CO_2$ values with depth, while others (e.g., LC5, AC1, and PBG2) display the opposite—decreasing values with depth.

Notably, the profiles CB3 (Fig. 9), LC5, and AC1 (Figs. 10 and 11) show heavier $\delta^{13}C\text{–}CO_2$ values at the shallowest sampled depth (10 cm), which gradually become lighter at greater depths (20–40 cm). Contrary to expectations, this pattern does not reflect natural vertical CO_2 gradients in the soil. Instead, the initial 10 cm measurement—collected immediately upon insertion of the stainless-steel sampling tube—likely captures the true deep hydrothermal signal. As the tube was progressively buried to reach greater depths, air contamination probably affected the samples, diluting the CO_2 and producing artificially lighter $\delta^{13}C\text{–}CO_2$ values. Therefore, the shallowest measurements are considered reliable, while the deeper samples may be influenced by this sampling artefact. Low soil permeability, as noted by Capasso et al. (2001), can exacerbate this effect by promoting air intrusion during sampling. Considering the difficulty of reaching depths beyond 20 cm at several sites in both calderas and the soil characteristics detailed in Section 2, this represents a major limiting factor for deeper measurements.

6. Conclusions

This work presents the first comprehensive coupling evaluation of stable carbon isotopes and CO_2 concentrations in vertical soil-gas profiles at the southern Puna's two largest silicic calderas, Cerro Blanco (CBC) and Cerro Galán (CGC). By integrating isotopic data with CO_2 concentration and flux measurements and applying a three-component mixing model, we quantified the relative contributions from three distinct CO_2 sources -deep hydrothermal, shallow (biogenic), and atmospheric-feeding the diffuse soil CO_2 emissions in these volcanic environments.

In CBC, high CO_2 concentrations (>5000 ppm) and $\delta^{13}C\text{-}CO_2$ values close to −5.2 ‰ (vs. V-PDB) indicates a dominant hydrothermal contribution, aligning with isotopic values reported for fumarolic emissions. Lower CO_2 concentrations (540–1300 ppm) and more depleted $\delta^{13}C\text{-}CO_2$ values (−15.4 to −11.6 ‰) reflected the influence of biogenic activity. Atmospheric contributions were minor but evident with intermediate $\delta^{13}C\text{-}CO_2$ values. In CGC, a broader range of $\delta^{13}C\text{-}CO_2$ values (−21.3 to −5.2 ‰) and CO_2 concentrations highlighted the interplay between hydrothermal and shallow sources, mainly at La Colcha and Aguas Calientes sites. Profiles from diffuse degassing structures (DDS) exhibited hydrothermal $\delta^{13}C\text{-}CO_2$ values (from −6.5 to −4.9 ‰), as expected for a higher-permeability zone that facilitates the ascent of deep-sourced fluids. In contrast, areas lacking DDS displayed lighter $\delta^{13}C\text{-}CO_2$ signatures (from −21.3 to −11.7 ‰), indicating dominant microbial CO_2 production.

Soil gas profiles revealed a wide variability in $\delta^{13}C\text{-}CO_2$ and CO_2 concentrations values. In both calderas, some site vertical trends partially deviate from the theoretical patterns of progressive deep $\delta^{13}C\text{-}CO_2$ enrichment. These deviations may result from multiple factors, including sampling-induced atmospheric contamination in low-permeability soils, low CO_2 fluxes promoting isotopic fractionation during diffusion, local secondary processes such as carbonate dissolution/precipitation or microbial activity, and methodological uncertainties at low efflux values. Nonetheless, the combined isotopic–concentration approach robustly confirms deep hydrothermal CO_2 contributions in shallow soil gases of CBC and CGC.

To further elucidate the mechanisms driving the observed isotopic composition variability in soil profiles, future research should improve the sampling device in low CO_2 flux areas and expand isotopic studies to other gases (e.g., CH_4, O_2, and N_2). These efforts are essential to refine our understanding of CO_2 degassing dynamics and their implications for geothermal exploration and volcanic monitoring in the Southern Puna, Central Andes region.

CRediT authorship contribution statement

A. Massenzio: Writing – review & editing, Writing – original draft, Visualization, Methodology, Investigation, Data curation, Conceptualization. **M.C. Lamberti:** Writing – review & editing, Writing – original draft, Methodology, Investigation, Data curation, Conceptualization. **A. Chiodi:** Writing – review & editing, Writing – original draft, Methodology, Investigation, Data curation, Conceptualization. **I. Burgos:** Writing – review & editing, Writing – original draft, Methodology, Investigation. **G. Viti:** Writing – review & editing, Writing – original draft, Methodology, Investigation. **F. Tassi:** Writing – review & editing, Writing – original draft, Methodology, Investigation, Formal analysis, Conceptualization. **M. Agusto:** Writing – review & editing, Writing – original draft, Investigation, Formal analysis, Conceptualization. **J. Viramonte:** Writing – review & editing, Writing – original draft, Investigation.

Declaration of competing interest

The authors declare that they have no known competing financial interests or personal relationships that could have appeared to influence

the work reported in this paper.

Acknowledgments

The fieldwork for this campaign was funded by the Project PICT 2019–03171 (IBIGEO; CONICET-UNSa), granted by the "Agencia Nacional de Promoción Científica y Tecnológica (Anpcyt) - Ministerio De Ciencia, Tecnología e Innovación Productiva" from Argentina. We thank the International Center for Earth Sciences of the Comisión Nacional de Energía Atómica, Argentina, for providing the Multigas device. We also wish to express our gratitude to Gladys Melián Rodríguez and Cecilia Amonte for kindly providing the vials used for soil gas sampling.

Appendix A. Supplementary data

Supplementary data to this article can be found online at https://doi.org/10.1016/j.jsames.2025.105828.

Data availability

Data will be made available on request.

References

Aravena, D., Muñoz, M., Morata, D., Lahsen, A., Parada, M.A., Dobson, P., 2016. Assessment of high enthalpy geothermal resources and promising areas of Chile. Geothermics 59, 1–13. https://doi.org/10.1016/j.geothermics.2015.09.001.

Arnosio, M., Becchio, R., Viramonte, J.G., Groppelli, G., Norini, G., Corazzato, C., 2005. Geología del Complejo Volcánico Cerro Blanco (26◦ 45' LS- 67◦ 45' LO), Puna Austral. In: Proceedings Geological Congress. La Plata, Argentina, pp. 851–858.

Báez, W., Arnosio, M., Chiodi, A., Ortiz Yañes, A., Viramonte, J.G., Giordano, G., Bustos, E., 2015. Estratigrafía y evolución del Complejo Volcánico Cerro Blanco, Puna Austral, Argentina. Rev. Mex. Ciencias Geol. 1, 29–49.

Báez, W., de Silva, S., Chiodi, A., Bustos, E., Giordano, G., Arnosio, M., Suzano, N., Viramonte, J.G., Norini, G. y, Groppelli, G., 2020a. Pulsating flow dynamics of sustained, forced pyroclastic density currents: insights from a facies analysis of the Campo de la Piedra Pomez ignimbrite, southern Puna, Argentina. Bull. Volcanol. 82, 53.

Báez, W., Bustos, E., Chiodi, A., Reckziegel, F., Arnosio, M., de Silva, S., Giordano, G., Viramonte, J.G., Sampietro-Vattuone, M.M., Pena-Monne, J.L., 2020b. Eruptive style and flow dynamics of the pyroclastic density currents related to the Holocene cerro blanco eruption (Southern Puna plateau, Argentina). J. S. Am. Earth Sci. 98, 102482.

Barcelona, H., Yagupsky, D.L., Wincour, D., Caselli, A., Cristallini, E.O., 2017. Modelo geológico estructural 3D del sistema geotérmico Copahue. In: Grosse, P. (Ed.), XX Congreso Geológico Argentino. Asociación Geológica Argentina, pp. 26–31. Tucuman.

Barry, P.H., de Moor, J.M., Giovannelli, D., Schrenk, M., Hummer, D.R., Lopez, T., 2019. Forearc carbon sink reduces long -term volatile recycling into the mantle. Nature 56 (8). https://doi.org/10.1038/s41586-019-1131-5 (7753), 48 7 –49 2.

Barry, P.H., De Moor, J.M., Chiodi, A., Aguilera, F., Hudak, M.R., Bekaert, D.V., Turner, S.J., Curtice, J., Seltzer, A.M., Jessen, G.L., Osses, E., Blamey, J.M., Amen 'abar, M.J., Selci, M., Cascone, M., Bastianoni, A., Nakagawa, M., Filipovich, R., Bustos, E., Schrenk, M.O., Buongiorno, J., Ramírez, C.J., Rogers, T.J., Lloyd, K.G., Giovannelli, D., 2022. The helium an d carbon isotop e characteristic s of th e andean convergent margin. Front. Earth Sci. 10, 897267. https://doi.org/10.3389/feart.2022.897267.

Barry, P.H., Hilton, D.R., Fischer, T.P., de Moor, J.M., Mangasini, F., Ramirez, C., 2013. Helium and carbon isotope systematics of cold "Mazuku" CO2 vents and hydrothermal gases and fluids from Rungwe Volcanic Province, Southern Tanzania. Chem. Geol. 339, 141–156. https://doi.org/10.1016/j.chemgeo.2012.07.003.

Baubron, J.C., Allard, P., Sabroux, J.C., Tedesco, D., Toutaln, J.P., 1991. Soil gas emanations as precursory indicators of volcanic eruptions. J. Geol. Soc. 148 (3), 571–576.

Bianchi, M., Heit, B., Jakovlev, A., Yuan, X., Kay, S.M., Sandvo l, E., Alonso, R., Coira, B., Brown, L., Kind, R., Comte, D., 2013. Teleseismic tomography of the southern Puna plateau in Argentina an adjacent region. Tectonophysics 58 (6), 65–83. https://doi.org/10.1016/j.tecto.2012.11.016.

Blair, N., Leu, A., Muñoz, E., Olsen, J., Kwong, E., Des Marais, D., 1985. Carbon isotopic fractionation in heterotrophic microbial metabolism. Appl. Environ. Microbiol. 50 (4), 996–1001.

Calixto, F.J., Sandvol, E., Kay, S., Mulcahy, P., Heit, B., Yuan, X., Coira, B., Comte, D., Alvarado, P., 2013. Velocity structure beneath the southern Puna plateau: evidence for delamination. G-cubed 14 (10), 4292–4305.

Camarda, M., De Gregorio, S., Favara, R., Gurrieri, S., 2007. Evaluation of carbon isotope fractionation of soil CO_2 under an advective–diffusive regimen: a tool for computing the isotopic composition of unfractionated deep source. Geochim. Cosmochim. Acta 71, 3016–3027.

Capasso, G., Favara, R., Inguaggiato, S., 1997. Chemical features and isotopic composition of gaseous manifestations on Vulcano Island, Aeolian Islands, Italy: an interpretative model of fluid circulation. Geochim. Cosmochim. Acta 61 (16), 3425–3440.

Capasso, G., D'Alessandro, W., Favara, R., Inguaggiato, S., Parello, F., 2001. Kinetic isotope fractionation of CO_2 carbon due to diffusion processes through the soil. In: Water-Rock Interaction, vol. 10. Swets & Zeitlinger, Lisse, pp. 1497–1499.

Carapezza, M.L., Granieri, D., 2004. CO_2 soil flux at Vulcano (Italy): comparison between active and passive methods. Appl. Geochem. 19, 73–88.

Cerling, T., Solomon, D., Quade, J., Bowman, J., 1991. On the isotopic composition of carbon in soil carbon dioxide. Geochem. Cosmochim. Acta 55, 3403–3405.

Chiodi, A., 2015. Caracterización geoquímica de sistemas geotérmicos en dos ambientes 520 contrastados del Noroeste Argentino: Puna Austral y Sistema de Santa Bárbara. Tesis doctoral. Universidad Nacional de Salta (Inédito) 229. Salta.

Chiodi, A., Tassi, F., Báez, W., Filipovich, R., Bustos, E., Glok Galli, M., Suzano, N., Ahumada, MaF., Viramonte, J.G., Giordano, G., Pecoraino, G., Vaselli, O., 2019. Preliminary conceptual model of the Cerro Blanco caldera-hosted geothermal system (Southern Puna, Argentina): inferences from geochemical investigations. J. S. Am. Earth Sci. 94, 102213.

Chiodi, A., Báez, W., Tassi, F., Bustos, E., Filipovich, R., Murray, J., Rizzo, A.L., Vaselli, A. O., Giordano, G., Viramonte, J.G., 2024. Fluid geochemistry of the Cerro Galán geothermal system (Southern Puna, Argentina): implications for the geothermal potential of one of the youngest giant calderas in the Andes. J. Volcanol. Geoth. Res. 450, 108089. https://doi.org/10.1016/j.jvolgeores.2024.108089.

Chiodini, G., Cioni, R., Guidi, M., Raco, B., Marini, L., 1998. Soil CO_2 flux measurements in volcanic and geothermal areas. Appl. Geochem. 13, 543–552.

Chiodini, G., Frondini, F., Cardellini, C., Granieri, D., Marini, L., Ventura, G., 2001. CO_2 degassing and energy release at Solfatara volcano, Campi Flegrei, Italy, Journal of Geophysical Research. Res. 106 (B8), 16,213 – 16,221, 2001.

Chiodini, G., Granieri, D., Avino, R., Caliro, S., Costa, A., 2005. Carbon dioxide diffuse degassing and estimation of heat release from volcanic and hydrothermal systems. J. Geophys. Res. 110, B08204. https://doi.org/10.1029/2004JB003542.

Chiodini, G., Caliro, S., Cardellini, C., Avino, R., Granieri, D., Schmidt, A., 2008. Carbon isotopic composition of soil CO_2 efflux, a powerful method to discriminate different sources feeding soil CO_2 degassing in volcanic-hydrothermal areas. Earth Planet Sci. Lett. 274 (3–4), 372–379.

Dawson, T.E., Mambelli, S., Plamboeck, A.H., Templer, P.H., Tu, K.P., 2002. Stable isotopes in plant ecology. Ann Rev Ecol Sys 33, 507–559.

Delph, J.R., Ward, K.M., Zandt, G., Ducea, M.N., Beck, S.L., 2017. Imaging a magma plumbing system from MASH zone to magma reservoir. EPSL 45 (7). https://doi.org/10.1016/j.epsl.2016.10.008, 31 3 –32 4.

Di Martino, R.M.R., Capasso, G., Camarda, M., 2016. Spatial domain analysis of carbon dioxide from soils on Vulcano Island: implications for CO2 output evaluation. Chem. Geol. 444, 59–70. https://doi.org/10.1016/j.chemgeo.2016.09.037.

Di Martino, R.M., Capasso, G., Camarda, M., De Gregorio, S. y, Prano, V., 2020. Deep CO_2 release revealed by stable isotope and diffuse degassing surveys at Vulcano (Aeolian Islands) in 2015–2018. J. Volcanol. Geoth. Res. 401, 106972.

Federico, C., Corso, P.P., Fiordilino, E., Cardellini, C., Chiodini, G., Parello, F., Pisciotta, A., 2010. CO_2 degassing at La Solfatara volcano (Phlegrean Fields): processes affecting $\delta^{13}C$ and $\delta^{18}O$ of soil CO_2. Geochim. Cosmochim. Acta 74, 3521–3538. https://doi.org/10.1016/j.gca.2010.03.010.

Fernandez-Turiel, J.L., Perez-Torrado, F.J., Rodríguez Gonzalez, A., Saavedra, J., Carracedo, J.C., Rejas, M., Lobo, A., Osterrieth, M., Carrizo, J., Esteban, G., Gallardo, J., Ratto, N., 2019. The large eruption 4.2 ka cal BP in Cerro Blanco, central volcanic zone, Andes: insights to the Holocene eruptive deposits in the southern Puna and adjacent regions. Estud. Geol. 75 (1), e088.

Filipovich, R., Chiodi, A., Báez, W., Ahumada, M.F., Invernizzi, C., Taviani, S., Aldega, L., Tassi, F., Barrios, A., Corrado, S., Groppelli, G., Norini, G., Bigi, S., Caricchi, C., De Benedetti, A., De Astis, G., Becchio, R., Viramonte, J.G., Giordano, G., 2022. Structural analysis and fluid geochemistry as tools to assess the potential of the Tocomar geothermal system, Central Puna (Argentina). Geothermics 98, 102297.

Folkes, C., Wright, H., Cas, R., de Silva, S., Lesti, C. y, Viramonte, J.G., 2011. A re-appraisal of the stratigraphy and volcanology of the Cerro Galán volcanic system, NW Argentina. Bull. Volcanol. 73 (10), 1427–1454.

Gilfillan, S.M.V., Sherwood Lollar, B., Holland, G., Blagburn, D., Stevens, S., Schoell, M., Cassidy, M., Ding, Z., Lacrampe-Couloume, G., Ballentine, C.J., 2009. Solubility trapping in formation water as dominant CO2 sink in natural gas fields. Nature 458.

Glamoclija, M., Garrel, L., Berthon, J., López-García, P., 2004. Biosignatures and bacterial diversity in hydrothermal deposits of Solfatara crater, Italy. Gomicrobiol. J. 21 (8), 529–541. https://doi.org/10.1080/01490450490888235.

Heit, B., Bianchi, M., Yuan, X., Kay, S.M., Sandvol, E., Kumar, P., Kind, R., Alonso, R.N., Brown, L.D., Comte, D., 2014. Structure of the crust and the lithosphere beneath the southern Puna plateau from teleseismic receiver functions. EPSL 38 (5), 1–11. https://doi.org/10.1016/j.epsl.2013.10.017.

Lamberti, M.C., Agusto, M., Llano, J., Nogués, V., Venturi, S., Vélez, Albite, J.M., Yiries, J., Chiodini, G., Cardellini, C., Tassi, F., García, S., Nuñez, N., Sánchez, H., Gomez, M., 2021a. Soil CO_2 flux baseline in Planchon ' – peteroa volcanic complex, southern Andes, Argentina. J. S. Am. Earth Sci. https://doi.org/10.1016/j.jsames.2020.102930.

Lamberti, M.C., Chiodi, A., Agusto, M., Filipovich, R., Massenzio, A., Báez, W., Tassi, T., Vaselli, O., 2021b. Carbon dioxide diffuse degassing as a tool for computing the thermal energy release at Cerro Blanco geothermal system, Southern Puna (NW Argentina). J. S. Am. Earth Sci. 105, 102833. https://doi.org/10.1016/j.jsames.2020.102833.

Lamberti, M.C., Nuñez, N., Velasquez Vargas, G., Pedreros Delgado, G., Llano, J., Massenzio, A., Bucarey Parra, C., Viti, G., Agusto, M., 2025. Soil carbon dioxide

diffuse emission during a volcano-tectonic seismic Swarm at Laguna del Maule volcanic field. J. S. Am. Earth Sci. 165, 105689. https://doi.org/10.1016/j.jsames.2025.105689. , ISSN 0895-9811.

Liang, X., Sandvol, E., Kay, S., Heit, B., Yuan, X., Mulcahy, P., Chen, C., Brown, L., Comte, D., Alvarado, P., 2014. Delamination of southern Puna lithosphere revealed by body wave attenuation tomography. J. Geophys. Res. Solid Earth 11 (9). https://doi.org/10.1002/2013JB010309 (1) , 54 9 –56 6.

Lucazeau, F., 2019. Analysis and mapping of an updated terrestrial heat flow data set. Geochem. Geophys. Geosyst. 20, 4001–4024. https://doi.org/10.1029/2019GC008389.

Lucic, G., Stix, J., Wing, B., 2015. Structural controls on the emission of magmatic carbon dioxide gas, Long Valley Caldera, USA. J. Geophys. Res. Solid Earth 120, 2262–2278. https://doi.org/10.1002/2014JB011760.

Ma, J., Wang, Z., Stevenson, B., Zheng, X. y, Li, Y., 2013. An inorganic CO_2 diffusion and dissolution process explains negative CO2 fluxes in saline/alkaline soils. Nature Scientific Reports 3, 2025. https://doi.org/10.1038/srep02025.

Ma, J., Li, Y. y, Liu, R., 2015. The abiotic contribution to total CO_2 flux for soils in arid zone. Biogeosci. Discuss. 12 (14), 11217–11244.

Massenzio, A., Chiodi, A., Lamberti, C., Murray, J., Filipovich, R., Salduondo, J., Nuñez, N., Gómez, M., Agusto, M., Viramonte, J., 2023. Estudio geoquímico y geológico en superficie del sistema geotermal Cerro Galán: desgasificación de CO_2, temperatura del suelo y alteración hidrotermal. In: Proceedings 18 ° Encuentro Del Centro Internacional De Ciencias De La Tierra (E -ICES 18), Argentina.

Massenzio, A., Chiodi, A., Lamberti, C., Murray, J., Filipovich, R., Salduondo, J., Agusto, M., Viramonte, J., 2024. Desgasificación difusa de dióxido de carbono y mineralización secundaria en los suelos del sistema geotermal Cerro Galán (Catamarca, Puna Austral). Rev. Asoc. Geol. Argent. 81 (2).

Melián, G., Hernández, P.A., Padrón, E., Pérez, N.M., Barrancos, J., Padilla, G., Dionis, S., Rodríguez, F., Calvo, D., Nolasco, D., 2014. Spatial and temporal variations of diffuse CO_2 degassing at El Hierro volcanic system: relation to the 2011–2012 submarine eruption. J. Geophys. Res. Solid Earth 119, 6976–6991. https://doi.org/10.1002/2014JB011013.

Panarello, H.O., Fernández, J.C., 2002. Stable carbon isotope measurements on hair from wild animals from altiplanic environments of Jujuy, Argentina. Radiocarbon 44, 709–716.

Pieber, S.M., Tuzson, B., Steinbacher, M., Emmenegger, L., 2021. Continuous Measurement of Stable CO_2 Isotopes at Jungfraujoch. Switzerland.

Raegan, P., Rogers, T.J., Fullerton, K.M., Selci, M., Cascone, M., Stokes, M.H., Steen, A. D., de Moor, J.M., Chiodi, A., Stefánsson, A., Halldórsson, S.A., Ramirez, C.J., Jessen, G.L., Barry, P.H., Cordone, A., Giovannelli, D., Lloyd, K.G., 2023. Complex organic matter degradation by secondary consumers in chemolithoautotrophy-based subsurface geothermal ecosystems. PLoS One 18 (8), e0281277. https://doi.org/10.1371/journal.pone.0281277.

Samec, C.T., Yacobaccio, H.D., Panarello, H.O., 2015. Carbon and nitrogen isotope composition of natural pastures in the dry Puna of Argentina: a baseline for the study of prehistoric herd management strategies. Archaeol. Anthropol. Sci. 9, 153–163.

Seggiaro, R., Hongn, F., Folguera, A., Clavero, J., 2000. Hoja Geológica 2769 – II. Paso De San Francisco. SEGEMAR. Boletín 294. Programa Nacional de Cartas Geológicas, 1:250.000.

Shanhun, F.L., Almond, P.C., Clough, T.J., Smith, C.M., 2012. Abiotic processes dominate CO2 fluxes in Antarctic soils. Soil Biol. Biochem. 53, 99–111.

Simmons, S.F., Christenson, B.W., 1994. Origins of calcite in a boiling geothermal system. Am. J. Sci. 294, 361–400.

Sinclair, A.J., 1974. Selection of threshold values in geochemical data using probability graphs. J. Geochem. Explor. 3, 129–149.

Stetter, K.O., 2006. Hyperthermophiles in the history of life. Philos. Trans. R. Soc. B 361, 1837–1843. https://doi.org/10.1098/rstb.2006.1907.

Stimac, J., Goff, F., Goff, C.J., 2015. Intrusion -Related geothermal systems. In: Sigurdsson, H. (Ed.), Encyclopedia of Volcanoes. Academic Press, pp. 79 9–82 2.

Tassi, F., Garofalo, P.S., Turchetti, F., De Santis, D., Capecchiacci, F., Vaselli, O., Cabassi, J., Venturi, S., Vannini, S., 2022. Insights into the Porretta Terme (northern Apennines, Italy) hydrothermal system revealed by geochemical data on presently discharging thermal waters and paleofluids. Environ. Geochem. Health 44 (7), 1925–1948.

Tieszen, L.L., 1991. Natural variations in the carbon isotopes of plants: implications for archaeology, ecology and paleoecology. J. Archaeol. Sci. 18, 227–248.

UNSa, 1982. Exploración Geotérmica En la Puna Salteña Y Cerro Galán – Salar De Antofalla, (Fase De Reconocimiento). Universidad Nacional de Salta (inédito). Salta.

Venturi, S., Tassi, F., Magi, F., Cabassi, J., Ricci, A., Capecchiacci, F., Caponi, C., Caponi, C., Nisi, B., Vaselli, O., 2019. Carbon isotopic signature of interstitial soil gases reveals the potential role of ecosystems in mitigating geogenic greenhouse gas emissions: case studies from hydrothermal systems in Italy. Sci. Total Environ. 655, 887–898.

Vignoni, P.A., Jurikova, H., Schröder, B., Tjallingii, R., Córdoba, F.E., Lecomte, K.L., Pinkerneil, S., Grudzinska, I., Schleicher, A., Viotto, S.A., Santamans, C.D., Rae, J.W. B., Brauer, A., 2024. On the origin and processes controlling the elemental and isotopic composition of carbonates in hypersaline Andean lakes. Geochem. Cosmochim. Acta 366, 65–83.

Viramonte, J.G., Castro Godoy, S., Arnosio, M., Becchio, R., Poodts, M., 2005a. El Campo geotermal de la Caldera de Cerro Blanco, utilización de Imágenes aster. In: Proceedings Geological Congress. Congreso Geológico Argentino, pp. 505–512. La Plata, Argentina. Actas del XVI.

Viramonte, J.G., Arnosio, M., Becchio, R., Gropelli, G., Norini, G., Corazzatto, C., DiFillipo, M., Blanco, M., Eulillades, P., Poodts, M., Castro Godoy, S., Klotz, J., Asch, G., Heit, B., 2005b. Cerro Blanco Volcanic Complex: the Youngest Caldera System in the Southern Central Andes. A Multidisciplinary Earth Science Project. Colloquium on Latin American Geosciences, Potsdam, p. 135.

Viveiros, F., Cardellini, C., Ferreira, T., Caliro, S., Chiodini, G., Silva, C., 2010. Soil CO_2 emissions at Furnas volcano, São Miguel Island, Azores archipelago: Volcano monitoring perspectives, geomorphologic studies, and land use planning application. J. Geophys. Res. 115, B12208. https://doi.org/10.1029/2010JB007555.

Wang, C., Wei, H., Liu, D., Luo, W., Hou, J., Cheng, W., Han, X., Bai, E., 2017. Depth profiles of soil carbon isotopes along a semi-arid grassland transect in northern China. Plant Soil 417, 43–52.

Ward, K.M., Delph, J.R., Zandt, G., Beck, S.L., Ducea, M.N., 2017. Magmatic evolution of a Cordilleran flare -up and its role in the creation of silicic crust. Sci. Rep. 7 (1), 9047. https://doi.org/10.1038/s41598-017-09015–5.